# Aerodynamic Characterization and Control of a Tail-Sitter Aircraft Taking Off in a Crosswind

Dylan Caverly

Department of Mechanical Engineering

McGill University
Montreal, Canada

April 2020

---

A thesis submitted to McGill University in partial fulfilment of the requirements of the degree of Master of Engineering.

# Abstract

The use of vertical take-off and landing (VTOL) vehicles is widespread for surveillance and rescue operations. Tail-sitters, a subset of VTOL vehicles, combine the maneuverability and ability to hover of quadrotors with the superior endurance and range of fixed-wing aircraft. The goal of this thesis is to address one of the shortcomings of tail-sitters—their high sensitivity to wind disturbances, especially in hovering configurations. To accomplish this, the aerodynamic forces and moments on a commercial tail-sitter were determined experimentally and then modelled. A real-time simulator was developed to incorporate the improved model aerodynamics. Next, a novel method to measure wind speed and direction is presented. Finally, two controller strategies were tested in the simulator environment to determine the aircraft's ability to reject wind disturbances in hovering missions through the use of feedforward control and path planning.

# Sommaire

L'utilisation de véhicules à décollage et atterrissage verticaux (VTOL) est très répandue pour les opérations de surveillance et de sauvetage. Les sous-ensembles, un sous-ensemble de véhicules VTOL, associent la maniabilité et la capacité de vol stationnaire des quadrimoteurs à l'endurance et à la portée supérieures des aéronefs à voilure fixe. Le but de cette thèse est de remédier à l'une des faiblesses des gardes de queue: leur grande sensibilité aux perturbations dues au vent, en particulier dans les configurations en vol stationnaire. Pour ce faire, les forces et les moments aérodynamiques sur une queue de selle commerciale ont été déterminés expérimentalement puis modélisés. Un simulateur en temps réel a été développé pour incorporer l'aérodynamique améliorée du modèle. Ensuite, une nouvelle méthode de mesure de la vitesse et de la direction du vent est présentée. Enfin, deux stratégies de contrôleur ont été testées dans l'environnement du simulateur afin de déterminer la capacité de l'appareil à rejeter les perturbations du vent dans les missions en vol stationnaire grâce à l'utilisation du contrôle anticipé et de la planification de trajectoire.

# Acknowledgements

First, I would like to acknowledge my supervisors. Professor Jovan Nedić's curiosity, insight, and open door policy were invaluable in the development of my work. I am grateful for his encouragement and support along the way. I would also like to thank Professor Meyer Nahon for his patience, feedback and guidance throughout my thesis.

The experimental setup was a thorough challenge that could not have been built alone. Thank you to Anushka Goyal for helping build our test facility, and Raphaël Limbourg for your technical support. Long days and late nights in the office passed quicker with you two, you're the best.

My thesis could not have been accomplished without the help of McGill's staff. My experimental setup was made with the help of McGill's technicians; Mathieu Beauchesne, Lydia Dyda and Miesam Aghajani from the Department of Mechanical Engineering, and David Speller from the Peter Guo-hua Fu School of Architecture. Thank you for your time and advice.

I greatly appreciate the financial support of the Natural Sciences and Engineering Research Council (NSERC) of Canada, and the Fonds de Recherche du Québec - Nature et Technologies (FRQNT), which made this work possible.

Finally, I would like to thank my parents, for their unconditional love and support, and my brother, Ryan, for his advice over the years.

# Contents

# List of Figures

# List of Tables

# Chapter 1

# Introduction

In recent years, unmanned aerial vehicles (UAVs) have become prevalent in society, with applications in both military and civilian fields, such as surveillance [1], rescue operations [2], tracking forest fires [3], and package delivery. Goldman Sachs forecasts that between 2016 and 2020, there will be a \$ 100 billion market opportunity for drones [4], with an estimated \$ 70 billion focused on military uses, \$ 17 billion focused on consumer uses, such as hobby drones, and \$ 13 billion associated with commercial and civil purposes, such as construction and agricultural surveillance, and police applications. One of the major obstacles that UAVs currently face is maintaining control during windy conditions, which will be the main focus of this thesis. However, before attempting to reject wind disturbances, we must select an appropriate type of UAV.

## 1.1 UAV Classification

In general, UAVs are classified by their size and purpose. However, there is no consensus on classification based on design. Most current UAV research focuses on small UAVs (SUAVs) , which are classified as weighing less than 20 kg, and generally have a wingspan on the order of $0.1 - 1$ m. One popular way to characterize UAV design is into fixed- and variable-geometry aircraft, as seen in Figure 1.1.

Fixed-geometry aircraft, such as conventional aircraft (fixed wing) and helicopters (fixed

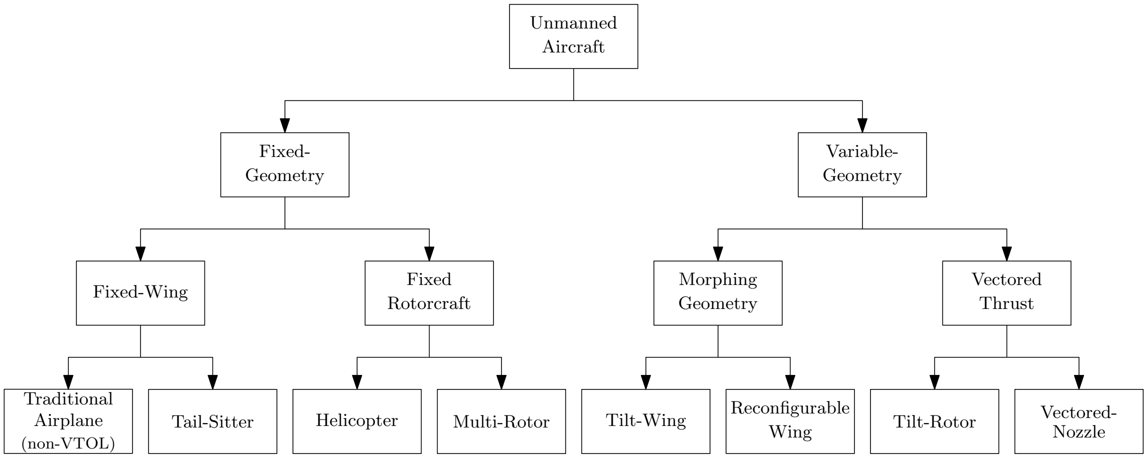

**Fig. 1.1**: UAV classification chart.

rotorcraft), only have control surfaces as the main moving parts. In both cases, propulsion is created by the rotation of a propeller. For fixed wing aircraft, *e.g.*, conventional airplanes, such as the McGill McFoamy (Figure 1.2(a)), or tail-sitters, such as the Wingtra tail-sitter (Figure 1.2(b)), the main source of lift is from the wing. The lift force for fixed rotorcraft on the other hand, such as helicopters and multi-rotors, both shown in Figure 1.3, come from the propellers directly.

Traditional airplanes are designed specifically for efficient forward flight. Therefore, besides a small minority that are specifically designed to do so, traditional airplanes are unable to perform aerobatic manoeuvres, such as quick and large changes in pitch or roll angle, or transitioning to hovering flight. As they can only apply thrust in the forward

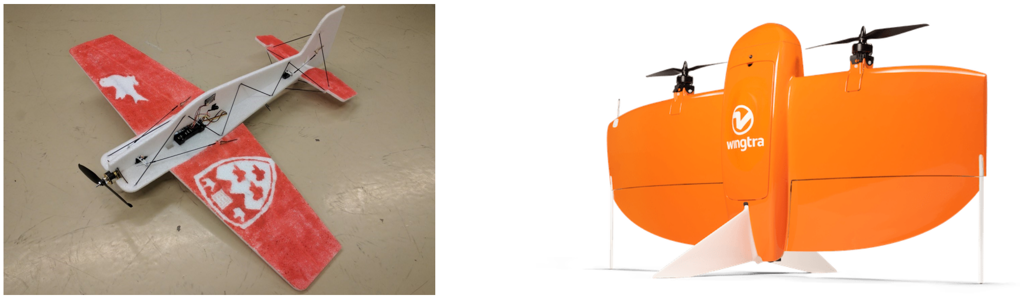
(a) (b)

**Fig. 1.2**: a) McGill McFoamy fixed-wing aircraft [5]. b) Wingtra tail-sitter [6].

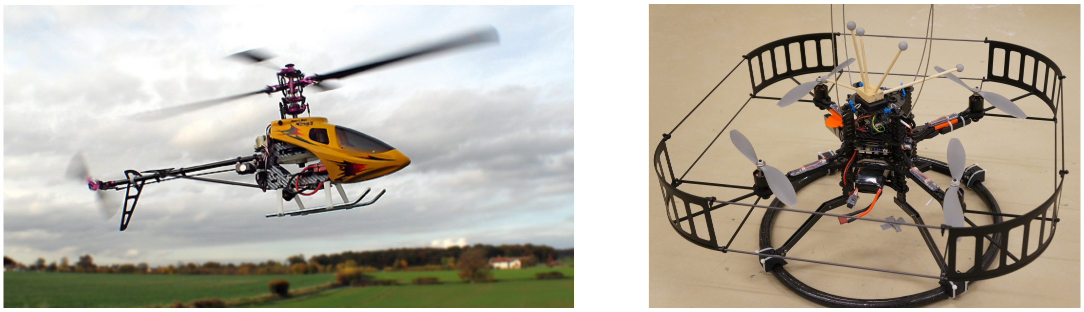
(a) (b)

**Fig. 1.3**: a) Remote-controlled helicopter [7]. b) AscTec Pelican quadrotor [8].

direction, and require the lift generated over their wings to take off, traditional airplanes require a runway of several multiples of the aircraft length to accelerate to the take-off speed. Similarly, long runways are required to land safely, which becomes and issue if an aircraft needs to take-off or land on a rough surface, such as mountainous areas, or in a place with limited runway space, such as rooftops.

One popular solution to the issue of a long runway requirement are vertical take-off and landing (VTOL) aircraft, which aircraft can take off and land in a smaller region, generally with an area roughly the size of the aircraft, such as a helicopter's helipad. Tail-sitter aircraft are a popular type of VTOL fixed-wing UAVs, such as the one shown in Figure 1.2(b). Tail-sitters take off in a nose-up orientation, after which they transition to horizontal cruising flight, and eventually back to vertical flight for landing. The transition to horizontal flight, and back to vertical, requires the tail-sitter to have high levels of aerobatic maneuverability. In addition, their large thrust-to-drag ratio (greater than 1, as compared to 0.3 for conventional aircraft), allows them to achieve hover flight.

Unlike fixed-geometry aircraft, variable-geometry aircraft have major aircraft components, such as wings or rotors, that can be reoriented mid-flight. In general, this is done on VTOL aircraft to redirect propellers or thrusters from a vertical orientation in take-off, hover, and landing, to a horizontal orientation for cruise. Vectored thrust UAVs, shown in Figure 1.4, redirect their thrusters to achieve this, while morphing geometry (Figure 1.5) rearrange entire lifting surfaces to change the direction of thrust.

(a) (b)

**Fig. 1.4**: a) TURAC Tilt-Rotor UAV [9]. b) Harrier Jump Jet [10].

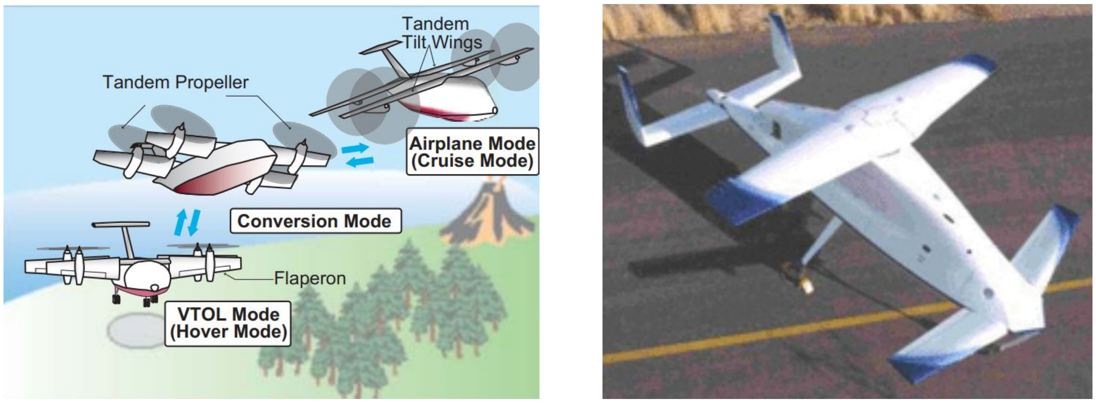

(a) (b)

**Fig. 1.5**: a) Tilt-Wing UAV [11]. b) Rotor-Wing UAV [12].

## 1.2 Design Selection

The general goals of this thesis are aimed at developing a controller architecture for a small-scale UAV, as well as studying and modelling its aerodynamic forces and moments. In order to select an appropriate UAV to model and control, several design criteria were set. First, an off-the-shelf, customizable, and programmable UAV should be selected. Since the focus of this thesis is not to design an aircraft itself, working with a readily available UAV will streamline the process, and common controllers will allow the implementation of manual control algorithms on the UAV. Second, designs that are commonly found in literature should be selected. The controller architecture and aerodynamic modelling developed in the thesis should be general enough to be transferred to other aircraft with similar geometry.

Less popular designs, such as tilt-wing, vectored-nozzle designs and reconfigurable-wing designs, were eliminated. Third, a UAV with lifting surfaces would be preferred. Since the aerodynamics of the system are of interest, fixed rotorcraft designs are not considered. Finally, due to the advantage of a smaller required take-off area, we decided to focus our efforts on VTOL UAVs. Therefore, traditional aircraft designs were eliminated.

With the specified constraints, the remaining configurations were tail-sitter and tilt-rotor UAVs. For each configuration, an off-the-shelf UAV was found that met all listed criteria: The X-Vert VTOL tail-sitter, made by Horizon Hobby, and the FireFLY6 tilt-rotor, made by BirdsEyeView Aerobotics.

### 1.2.1 Platform Selection

The FireFLY6 tilt-rotor, shown in Figure 1.6, has a blended wing-body design. This aircraft contains an open-source Pixhawk controller, allowing for easy programming. This design uses three pairs of counter-rotating propellers. In hover and vertical manoeuvres, the two pairs of front propellers are oriented vertically, and can tilt to a horizontal orientation to transition to horizontal flight, while the rear pair is always fixed upwards.

**Fig. 1.6**: FireFLY6 tilt-rotor UAV from Horizon Hobby.

The X-Vert VTOL tail-sitter, shown in Figure 1.7, has a blended wing-body design and a wing span of approximately 0.5 m. The blended wing-body design is a tailless aircraft. As a result, instead of having ailerons on its wings and elevators on its tail, it has a single control surface on the trailing edge of each wing, known as elevons. The X-Vert has two propellers, fixed in a forward direction in the body frame. In order to transition to horizontal flight, the aircraft uses its elevons to pitch its entire body forward into a horizontal attitude. Out of the box, the X-Vert tail-sitter includes its own basic controllers,

**Fig. 1.7**: X-Vert VTOL tail-sitter.

which can be easily replaced with a Pixhawk controller, allowing for the implementation of custom-built controllers.

Ultimately, the X-Vert VTOL tail-sitter was selected as the aircraft to study. The tail-sitter design is mechanically simpler as its propellers cannot tilt, therefore risking fewer mechanical failures. Next, the tilt-rotor design undergoes high drag forces in vertical flight, such as take-off and landing, which reduce aircraft efficiency. With large drag forces, the aircraft will have to apply much more thrust to take off and land than a tail-sitter. In vertical flight and hover, the tail-sitter orientation should have more control authority than the tilt-rotor, as larger forces and moments can be applied by elevon deflections downstream of the propellers, allowing the aircraft to make aerobatic manoeuvres.

### 1.2.2 Tail-sitter Overview

One of the earliest tail-sitter designs to take flight was the Convair XFY-1 “Pogo” in 1954, shown in Figure 1.8(a). This project was cancelled soon after its first flights, in part due to complications associated with transitioning from vertical to horizontal flight, and the difficulty to land due to the pilot’s orientation within the aircraft [13]. In order to transition between horizontal and vertical flight, strong pitching moments must be performed, which could not always be created with the limited control authority of the aircraft ailerons. Military designs for hybrid VTOL aircraft soon shifted towards vectored thrust designs, such as the Harrier Jump Jet. These designs were much more mechanically com-

(a) (b)

**Fig. 1.8**: a) The Convair XFY-1 [14]. b) The Bell APT tail-sitter [15].

plex than the Convair XFY-1, as they involved more moving parts to reorient the aircraft's thrust. Nonetheless, these newer designs were preferred as they could be better handled by pilots, as pilots no longer had to look behind them in order to land.

Since 1954, sensor precision has improved significantly, as well as control and estimation strategies, allowing for the emergence of autonomous aircraft with any type of geometry and design. With these advancements, the limitations of pilots' capabilities no longer prevent tail-sitters from being a viable type of aircraft, as they can fly autonomously. Bell Helicopter is currently developing the Bell Autonomous Pod Transport (APT) series of tail-sitters for transporting cargo [15], as seen in Figure 1.8(b).

One main application of UAVs is for surveillance, such as monitoring construction sites or forest fires, which requires the aircraft to hover. When flying outdoors, however, the aircraft is susceptible to wind gusts, which fluctuate in both magnitude and direction, causing the aircraft to lose stability and control. While cruising horizontally, small UAVs with wingspans on the order of 1 m can often reach speeds of 20 m/s. When dealing with winds of 6 m/s, which are characterized as a moderate breeze on the Beaufort Scale [16], the disturbance forces associated with such wind are manageable. However, for UAVs in other orientations, a moderate breeze can have a more significant effect on the aircraft, particularly during hovering flight.

UAVs that hover and achieve vertical flight with a nose-up orientation, such as tail-sitters, are particularly affected by wind disturbances. If a small hovering tail-sitter is normal to winds of 6 m/s, the drag force acting on the aircraft can generate large aerodynamic forces and moments, possibly larger than the thrust generated by its propellers. These forces and moments can cause significant acceleration and moments, causing a hovering tail-sitter to deviate far from its intended position. That said, if a hovering tail-sitter was aligned with the flow, such that its body was parallel to the wind direction, it should experience much smaller aerodynamic forces or moments. The same holds on take-off and landing, where a tail-sitter may struggle to maintain its position or follow a desired path more than a tilt-rotor aircraft, and the tail-sitter will incur stronger body forces from the wind if it is normal to the flow rather than parallel to it.

On its packaging, the X-Vert states that with its proprietary controllers, when flying outdoors in “moderately windy” conditions, only horizontal flight should be attempted. In its attached manual, the manufacturer recommends hovering and flying vertically only in “very light or no wind”. It also suggests that, if manually hovering the tail-sitter via a remote controller, aircraft position can be somewhat maintained in moderate winds by “experienced pilots” by rolling the aircraft, such that its body is aligned with the wind.

Considering this information, the scope of this thesis is narrowed. The main goal of this thesis is to model, control and simulate the flight path of an X-Vert tail-sitter in windy conditions. Specifically, we want to investigate the relative benefit of orienting the aircraft with the wind direction, during nose-up operation, *i.e.*, during hover, take-off and landing.

## 1.3 Literature Review

### 1.3.1 Wind Tolerant UAV Control and Wind Estimation

Most existing UAV wind rejection control strategies are general, in that they design controllers to reject any unknown force and moment disturbances, rather than the specific forces and moments that originate from oncoming winds. For example, in [17], an $\mathcal{H}_\infty$ controller is implemented on a quadrotor to reject any model uncertainties.The wind disturbances are modelled as step forces and step moments, and rejected, as the controller maintains a desired position despite the disturbances. In [18], a nonlinear adaptive controller is designed for a quadrotor to be robust to constant force disturbances, and is tested in the presence of a constant wind flow from an electric fan to evaluate the controller performance. The controller successfully reduces position error while the quadrotor aircraft tracks a given trajectory. Although these systems model and reject a disturbance, the disturbance is not necessarily reflective of real wind effects, which will fluctuate in both magnitude and direction over time.

The most popular wind models found in literature to simulate wind gusts are the Dryden wind turbulence model [19] and the von Karman wind turbulence model. Both provide mathematical models for the power density spectrum based on turbulent length scales and the aircraft altitude. Both models have applications in MATLAB Simulink, allowing them to be easily implemented to model wind gusts in a simulation framework. The Dryden wind turbulence model is more simple mathematically, and is the more common of the two models [20–22].

Recent studies [23–26] have attempted to design controllers for UAVs that directly reject the forces and moments from wind disturbances. In order to do this, the controller must have some knowledge of the wind passing over the aircraft. Currently, there is no method to accurately determine the wind magnitude and direction passing over a small tail-sitter UAV. Wind measurements recorded on the ground do not necessarily reflect the wind passing over a UAV, as wind fields are not uniform and steady. Nonetheless, some options are being considered to accurately estimate oncoming wind speed and direction.

In [23], the aerodynamic forces and moments from wind passing over a quadrotor are estimated using measurements from an on-board inertial measurement unit (IMU). The IMU measures the acceleration and attitude of the aircraft, and any unexpected acceleration and rotations of the aircraft are assumed to be results of wind forces and moments acting on the body. Their work uses these forces and moments to estimate the wind speed and direction. In simulations, they estimate the oncoming wind velocity vector within approximately $20\%$ of the simulation values, and use this information to allow a quadrotor to hover in a desired location under 2 m/s winds. Their addition of this wind estimation halved their mean position error over their flight. However, the authors recognize that their simulation model considers a simplified model for the quadrotor aerodynamics, which does not consider real-world uncertainties, such as specific drag coefficients associated with their quadrotor geometry, and sensor uncertainty from IMU data.

In [24], six pairs of pressure probes are placed on a quadrotor to estimate relative wind speed. These pressure probes are placed externally on the UAV, far enough from the propellers to reduce interaction with their downwash. This effectively increases both the span and height of the quadrotor, and will affect its aerodynamic performance and stability. To our knowledge, this has not yet been tested on any aircraft other than rotorcraft.

The use of feedforward control has been used to reject disturbances. If there is knowledge of the disturbance properties, the addition of feedforward control to feedback controllers can reduce transient error [25]. Tran and Nahon [26] have used feedforward controllers in addition to both PID and linear-quadratic-regulator (LQR) controllers to reduce transient position error when a wind gust is introduced to a quadrotor aircraft. In MATLAB Simulink simulations, the addition of feedforward controllers resulted in a significant performance increase, reducing position error by approximately an order of magnitude. However, in laboratory experiments, the addition of feedforward control provided a negligible improvement to aircraft performance, which was likely a result of noisy wind sensors, which provided the quadrotor with unreliable information about wind speed and direction. With more precise wind sensors, it is likely that pairing feedforward with feedback controllers will improve UAV performance.

### 1.3.2 Existing Tail-Sitter Research

The T-Wing tail-sitter at the University of Sydney has been shown to fly and hover, while able to reject wind disturbances of up to 9 m/s. This aircraft has a wingspan of 2.2 m and a mass of 29.5 kg [27]. This UAV was tested with several several controllers, including PID controllers, quaternion-based attitude control, and an LQR controller [27–30]. Due to its relatively large mass, the T-Wing tail-sitter is less affected by wind disturbances than smaller aircraft. In comparison, the X-Vert tail-sitter has a span of 0.5 m, and a mass of 0.2 kg.

A large portion of ongoing tail-sitter research focuses on modelling and controlling a tail-sitter in its transition between vertical and horizontal flight [29, 31–33]. Since many tail-sitters have configurations similar to agile aircraft, their aerodynamics in horizontal cruising flight has largely been studied for agile aircraft, which can translate well to tail-sitters with similar geometry.

In [34], a quaternion-based proportional-integral-derivative (PID) controller is designed for agile hovering fixed-wing UAVs. Their work assumed a previous impulse disturbance, such as a wind gust, caused a large change in attitude from its initial orientation. Under windless conditions, the controller successfully returned the hovering UAV to its desired orientation.

Recently, Chiappinelli and Nahon [35] developed a flight simulator for the X-Vert tail-sitter. This model works with a semi-empirical relationship for flat plates to model the tail-sitter aerodynamics. This model is further discussed in Section 2.3.3. The work also proposes a universal quaternion-based PID feedback controller, which simultaneously controls aircraft position and attitude, which will be further discussed in Section 4.1. In their work, they recognize that their aerodynamic model required validation through wind tunnel experiments, as they did not have access to one in their research. With incorrect aerodynamics, developments made in the simulation framework may not be reflective of real-world applications.

## 1.4 Thesis Objectives

The objectives of this thesis are as follows:

1. To perform wind tunnel tests aimed at verifying the validity of the tail-sitter aerodynamic model used in [35].
2. To evaluate the potential benefit of aligning the aircraft with the wind when in a nose-up configuration, using the simulation developed in [35].
3. To evaluate the use of feedforward control to reject wind disturbances, using the simulation developed in [35].
4. To propose new methods to estimate wind speed and direction relative to a UAV.

## 1.5 Thesis Organization

This thesis is structured as follows. Chapter 2 reviews the experimental methods used to validate the tail-sitter's existing aerodynamic model. Chapter 3 presents a novel approach to estimating wind magnitude and direction. Chapter 4 presents the simulation platform used to model and control the aircraft. The addition of feedforward to feedback control is evaluated, as well as several paths to better reject wind disturbances for a hovering tail-sitter.

# Chapter 2

# Aerodynamic Loads on X-Vert Aircraft

In a previous study, Chiappinelli and Nahon [35] developed a semi-empirical model of the aerodynamic forces and moments acting on the same X-Vert aircraft studied here based on the approach of Khan and Nahon [36]. As the X-Vert tail-sitter has a flying-wing configuration, with thin airfoils, the simulation in [35] treats the tail-sitter as a collection of flat plates, and considers the air passing over them. This application of the semi-empirical relationship, however, only considered aerodynamic forces applied in the longitudinal plane, *i.e.*, forces that may cause pitching moments, and neglected forces along the body $y$-axis, or any associated rolling or yawing moments. With most traditional aircraft simulators, this is sufficient, as when an aircraft is cruising in horizontal flight, forces along the body $y$-axis are negligible compared to forces in the longitudinal plane. However, when a tail-sitter is hovering, wind disturbances can cause large forces normal to the aircraft planform, and large moments about the rolling axis, which would need to be accurately accounted for in order to better simulate and control the aircraft.

Since the model assumes that all lifting surfaces are flat plates, in this chapter, we test a flat-plate acrylic version of the X-Vert tail-sitter in a wind tunnel to determine whether the experimental data and the semi-empirical model data are comparable. Additionally, we measure rolling moments, and forces along the body $y$- axis, to account for any omissions in the model of [35]. This is first accomplished by validating the existing semi-empirical aerodynamic model for forces in the longitudinal plane and pitching moments, then developing a new model for forces in the body $y$-$z$ plane, as well as rolling moments that will eventually be incorporated into the controller.

## 2.1 Experimental Setup

### 2.1.1 Wind Tunnel Configuration

All measurements in this thesis were performed in the Newman wind tunnel in the McGill University Department of Mechanical Engineering Aerodynamics Laboratory, shown in Figure 2.1. This low-speed wind tunnel has a test section with a constant cross-sectional area of 2’×3’ (0.61 m × 0.91 m) and is 6’ (1.83 m) long. The top speed of the wind tunnel in the test section is $30$ m/s. The wind speed is controlled by a CFW-08 frequency inverter, from WEG Industries. The wind tunnel has a background turbulence level of $1.1\%$ at a freestream velocity of $10$ m/s.

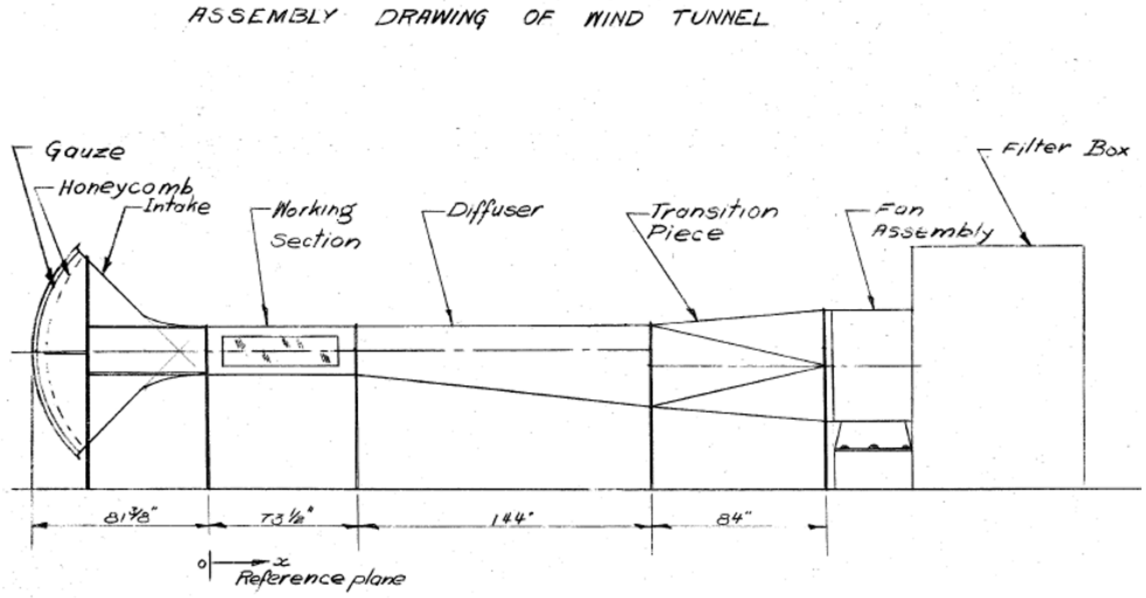

Fig. 2.1: Newman wind tunnel at McGill University [37].

In order to determine where to place items in the test section of the wind tunnel, such as the acrylic model and any measurement probes, the boundary layer thickness should be estimated, so that the items are placed far enough away from the boundary layer flow. Assuming fully turbulent flow from the inlet, a maximum freestream velocity of $U =$

$20$ m/s, and that the experimental model is placed $3$ m ($\sim$ $117$ in) downstream of the inlet, in the centre of the test section, the boundary layer thickness $\delta$ on the walls of the test section can be approximated to be $\delta = 0.37xRe_x^{-1/5} = 5.3$ cm [38], where $Re_x = \frac{Ux}{\nu} = 4.2 \times 10^6$. This is likely a slight overestimate of the boundary layer thickness, given that the boundary layer is unlikely to be turbulent from the start of the inlet.

In order to determine the wind speed in the tunnel, a Pitot-static tube was placed upstream of the experimental setup. It was placed $18$ cm from the wind tunnel floor and $25$ cm from the side-wall, so that the pressure measurements are not influenced by the boundary layer growing on the walls of the test section, while in a position such that slipstream behind the Pitot-static probe should not interact with the rest of the experimental setup. The pressure differential from the Pitot-static probe was measured by a Furness Controls FCO332 differential pressure transducer. The FCO332 can read pressure differences between $0$ and $500$ Pa, with an accuracy within $0.25\%$ of readings, and a sensitivity of $100$ Pa/V. The pressure transducer outputs a voltage, which was acquired by a National Instruments USB-6363 X Series Data Acquisition (DAQ) Unit with BNC pinout, which was then converted to a pressure with a linear conversion rate of $100$ Pa/V. The readings from the pressure transducer, as well as a 3-wire $100$ Ohm Resistance Thermometer Detector (RTD), were used to calculate the air density and freestream wind velocity, using the Ideal Gas Law, and Bernoulli's equation, respectively, $\rho = p_{atm}(R_{specific}T)^{-1}$, and $U = \sqrt{2\Delta p\rho^{-1}}$, where $\rho$ denotes the air density, $p_{atm}$ denotes absolute atmospheric pressure, $R_{specific} = 287.06\frac{J}{kg \cdot K}$ is the specific gas constant of air, $T$ is the air temperature in the wind tunnel, $U$ is the freestream velocity, and $\Delta p$ is pressure difference across the Pitot-static tube.

To measure atmospheric pressure, a Honeywell Model TJE Precision Gage/Absolute Pressure Transducer, rated for $100$ psig, was purchased. Unfortunately, the absolute pressure transducer could not receive the proper excitation voltage from the National Instruments compact Data Acquisition Unit (cDAQ)-9174. Instead, the atmospheric pressure was assumed to be standard atmospheric pressure, $101.35$ kPa.

**Fig. 2.2**: FCO332 differential pressure transducer by Furness Controls.

### 2.1.2 Wind Tunnel Model

The X-Vert tail-sitter has a planform area of 775 cm$^2$. This was initially approximated by Chiappinelli [35], and validated in this thesis by using a FARO Arm 3D scanner, to generate a more precise 3D model of the aircraft, as seen in Figures 2.3 and 2.4. These scans were performed by technicians at the Additive Manufacturing Lab at McGill University. When normal to the wind direction, the planform area of the tail-sitter is 14% of the wind tunnel cross-sectional area.

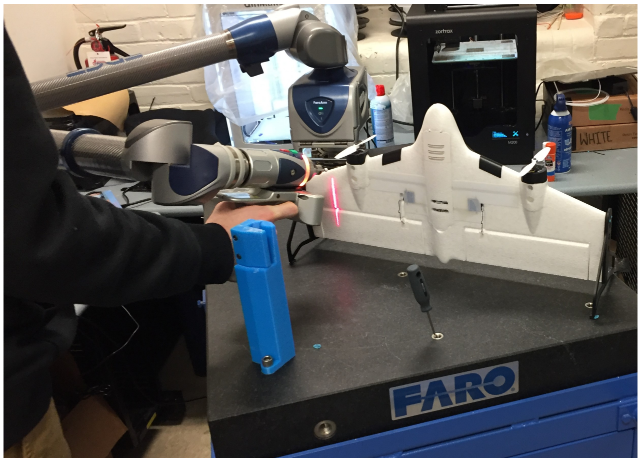

**Fig. 2.3**: Virtual model of X-Vert tail-sitter, generated by FARO Arm scans.

If an object in a wind tunnel is large relative to the wind tunnel's cross-sectional area, the blockage creates a nozzle effect, and the air passing over it will speed up due to the smaller free cross-sectional area within the tunnel. Barlow, Rae and Pope [39] suggest that

**Fig. 2.4**: X-Vert tail-sitter being scanned with a FARO Arm.

the increase in velocity can be approximated by one quarter of the ratio of the blockage's frontal area to the cross-sectional area of the wind tunnel. Therefore, if the full-size tail-sitter were placed in the wind tunnel, the wind speed would increase by $3.5\%$. Barlow, Rae and Pope [39] recommend maintaining a blockage ratio below $5\%$ to reduce blockage effects. Therefore, a full-scale model of the X-Vert could not be tested within the wind tunnel. Instead, a flat-plate half-scale model of the X-Vert tail-sitter was made out of a 6mm thick acrylic plate by laser cutting the planform profile, using a Universal Laser System VLS 6.60, available at the Peter Guo-hua Fu School of Architecture at McGill University. The laser-cut acrylic model is shown in Figure 2.5.

With all dimensions halved, the flat plate's surface area is quartered, resulting in a $3.5\%$ blockage ratio. This smaller blockage ratio will lead to a velocity increase of $0.75\%$. This flat plate will provide a reasonable approximation to validate and model the aerodynamic forces and moments acting on the tail-sitter.

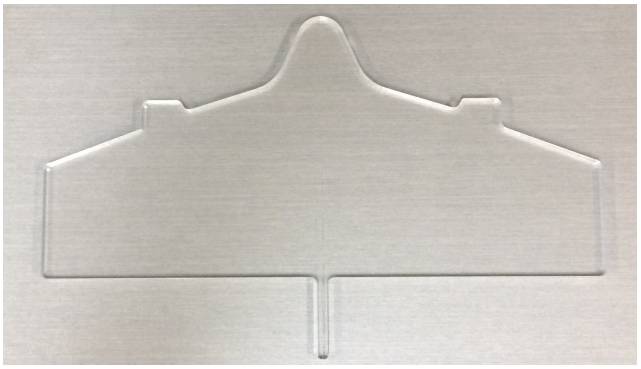

**Fig. 2.5**: Tail-sitter flat plate acrylic model.

**Table 2.1**: Properties of half-scale tail-sitter acrylic flat-plate model.

| | |
|---|---|
| Area ($S$) | 194 cm$^2$ |
| Span ($b$) | 25 cm |
| Chord (root) ($c_r$) | 11.7 cm |
| Chord (tip) ($c_b$) | 4.8 cm |
| Mean Aerodynamic Chord ($\bar{c} = S/b$) | 7.76 cm |
| Characteristic length ($\sqrt{S}$) | 13.9 cm |
| Aspect Ratio ($b^2/S$) | 3.2 |
| Thickness ($t$) | 6 mm |

To measure the aerodynamic forces and moments acting on the acrylic flat plate model, the acrylic plate was mounted onto a Gamma IP68 six-axis force/torque sensor by ATI Industrial Automation. All specifications are provided in Table 2.2 and Table 2.3. The acrylic model was not mounted directly onto the force/torque sensor, but rather indirectly through custom-made 3D printed fixtures, and a $3/8$”-diameter steel rod, with a length of $25$ cm, such that the acrylic model is set at the centre of the wind tunnel’s cross section. The force/torque sensor was then mounted onto a Newmark Systems RM-3D-411-NC rotary stage via a $6$ mm thick aluminium plate. The rotary stage has a rotational resolution of $\pm 0.002°$. In order to connect the flat plate model to the steel rod, and the steel rod to the force/torque sensor, custom fixtures were 3D printed, as seen in Figure 2.6, and screwed together, as seen in Figures 2.7 to 2.10. All 3D printed fixtures were made on a Formlabs Form 2, a stereo-lithography printer, with a layer resolution of $0.025$ mm, using their proprietary Standard Black V4 photopolymer resin.

**Table 2.2**: ATI Gamma IP68 Calibrated Range ($\pm$)

| $\mathbf{F}_x$ | $\mathbf{F}_y$ | $\mathbf{F}_z$ | $\mathbf{T}_x$ | $\mathbf{T}_y$ | $\mathbf{T}_z$ |
|---|---|---|---|---|---|
| 32 N | 32 N | 100 N | 2.5 N-m | 2.5 N-m | 2.5 N-m |

The force sensor and pressure transducer data was collected by the National Instruments 6363 USB Data Acquisition Unit, while the RTD data was collected by a National Instruments compact Data Acquisition Unit (cDAQ)-9174. All data was then acquired via LabVIEW. Before every experiment, the pressure transducer and RTD were used to determine the freestream velocity by acquiring data at $1000$ Hz for $2$ s. Measurements from the

**Table 2.3**: ATI Gamma IP68 Measurement Uncertainty ($95\%$ confidence level, percent of full-scale load)

| $\mathbf{F}_x$ | $\mathbf{F}_y$ | $\mathbf{F}_z$ | $\mathbf{T}_x$ | $\mathbf{T}_y$ | $\mathbf{T}_z$ |
|---|---|---|---|---|---|
| $0.75\%$ | $1.00\%$ | $0.75\%$ | $1.00\%$ | $1.00\%$ | $1.50\%$ |

force/torque sensor were taken at a sampling rate of $1000$ Hz for $30$ s.

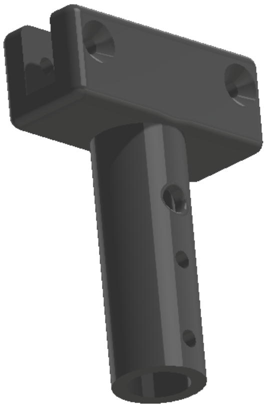

**Fig. 2.6**: Sample fixture used to connect acrylic plate to steel rod.

### 2.1.3 Pitching Rotation

To measure the aerodynamic forces and moments due to pitching, the flat plate model was mounted such that its planform was oriented vertically, with its nose pointing radially outward from the mounting rod, as seen in Figures 2.7 and 2.8. At a pitch angle of $0°$, the nose is pointed into the wind, while at a pitch angle of $90°$, the nose is pointed orthogonal to the wind direction.

### 2.1.4 Rolling Rotation

To measure the aerodynamic forces and moments due to rolling, the flat plate model was mounted such that its planform was oriented vertically, as seen in Figures 2.9 and 2.10 with its longitudinal axis pointing vertically. At a roll angle of $0°$, the flat plate is aligned with the wind. At a roll angle of $90°$, the flat plate is normal to the wind.

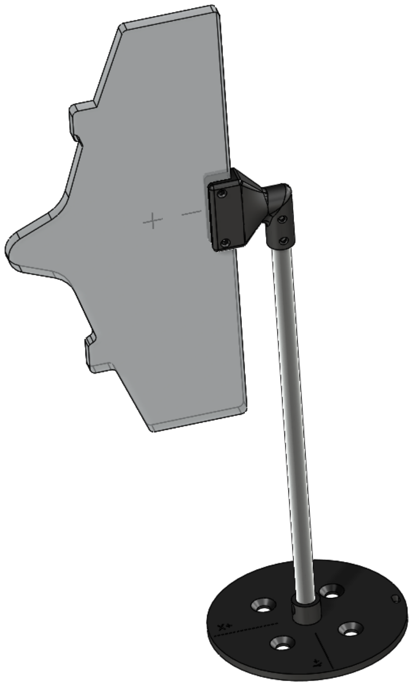

**Fig. 2.7**: Experimental setup to validate forces and moments at different pitch angles.

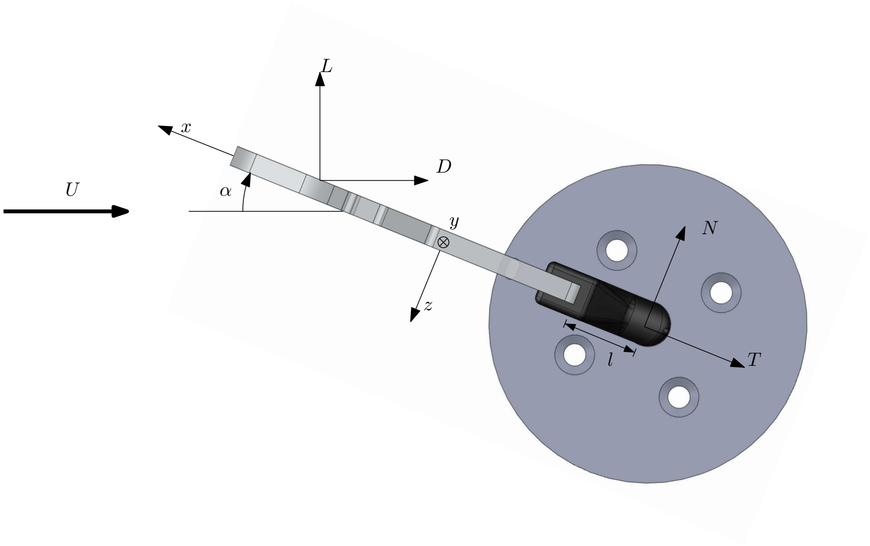

**Fig. 2.8**: Top view diagram of pitching assembly setup.

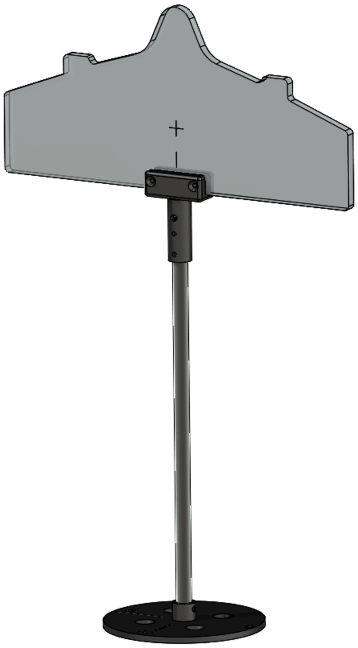

**Fig. 2.9**: Experimental setup to validate lift, drag, and rolling moments at different roll angles.

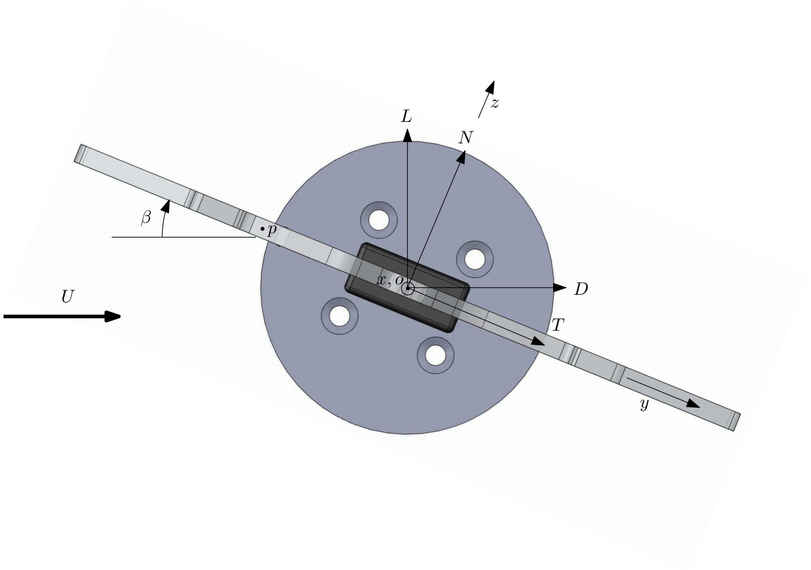

**Fig. 2.10**: Top view diagram of rolling assembly setup.

## 2.2 Experimental Procedure

With the experimental system set up, data was then acquired. Before each run, the zero angle of the setup was determined. With the wind tunnel at the desired speed, the rotary stage was swept over a small range of $\pm\, 10°$ around an approximate zero, and force/moment data was acquired. The normal and tangential forces to the plate were considered, and the angle corresponding to a zero normal force was defined as the $0°$ orientation. Since the test stand was very sensitive to external disturbances, the $0°$ orientation had to be determined before every test.

For both the pitching and rolling tests, measurements were taken in orientations between $-50°$ to $100°$ in $2°$ increments, where $0°$ is defined as the orientation where the flat plate is aligned with the flow, and $90°$ where the flat plate is perpendicular to the flow. At each angle, the LabView program waited $10$ s, allowing transient forces and moments to dissipate, and then recorded $30$ s worth of data at a rate of $1000$ Hz from the force/torque sensor.

When exposed to the flow in the test section, the force/torque sensor measures the aerodynamic forces and moments acting on the flat plate model and the supporting rod. In order to remove the forces and moments from the supporting rod, *i.e.*, bias measurements, a set of preliminary measurements was taken at each wind speed and angle with the flat-plate model of the X-Vert removed. This data was then subtracted from the full data set. Since only the mean forces and moments were considered, no filters were applied to the data set.

### 2.2.1 Wind Speed Selection

When considering the full-sized tail-sitter hovering in cross-winds, wind speeds of $2.5$–$7.5$ m/s were desired. These are characterized within the Beaufort Scale [16] as ranging from a light breeze to a moderate breeze. The full-sized tail-sitter has a planform surface area of $S = 776$ cm$^2$, which has a characteristic length $\sqrt{S} = 27.9$ cm, which corresponds to Reynolds numbers on the order of $Re = 50,000 - 150,000$.

Since the flat plate model is half the size of the original model, in order to keep a consistent Reynolds number ($\frac{Ul}{\nu}$), the speed in the wind tunnel had to be doubled. Therefore, instead of observing between $0$–$10$ m/s winds, wind tunnel speeds between $0$–$20$ m/s were considered. The plate was observed to vibrate in its fixture in the pitching setup at a freestream velocity of $20$ m/s, and in the rolling setup at freestream velocities above $15$ m/s. Therefore, experiments were conducted at freestream velocities of 5, 10, and 15 m/s for the pitching setup. These speeds correspond to Reynolds numbers on the order of $50,000, 100,000$ and $150,000$, respectively, based on the characteristic length of the scaled plate, defined as the square root of the planform area, $\sqrt{S} = 13.9$ cm. Similarly, experiments on the rolling setup were performed at freestream velocities of 5 and 10 m/s, corresponding to Reynolds numbers $Re = 50,000$ and $100,000$. Ideally, if the experimental data collapses onto the same curve, it will be safe to assume that the results for the full scale model will also collapse onto the same curve.

## 2.3 Data Preprocessing

As only force and moments were considered in this section, aerodynamic coefficients were calculated by

$$\begin{aligned} C_L &= \frac{2L}{\rho U^2 S}, \\ C_D &= \frac{2D}{\rho U^2 S}, \\ C_M &= \frac{2M}{\rho U^2 S \bar{c}}, \end{aligned}$$

where $\rho$ is the air density, $S$ is the flat plate area, $U$ is the wind tunnel velocity and $\bar{c} = S/b$ is the mean aerodynamic chord. The lift force, denoted by $L$, is the force perpendicular to the wind direction, while the drag force, denoted by $D$, is the force parallel to the wind direction. Finally, the moment $M$ is the moment about the mounting rod. In the pitching rotation setup, $M$ corresponds to the pitching moment of the flat plate, while in the rolling rotation setup, it corresponds to the rolling moment.

### 2.3.1 Force Corrections

Due to the experimental setup, the lift and drag forces could not be directly measured. Instead, the force/torque sensor outputs tangential and normal forces on the flat plate. Corrections have to be made to convert the normal and tangential forces to lift and drag forces,

$$\begin{aligned} L &= N\cos\alpha - T\sin\alpha, \\ D &= N\sin\alpha + T\cos\alpha. \end{aligned}$$

Here, $N$ corresponds to the forces normal to the plate, $T$ represents the tangential forces acting on the plate, aligned with the sensor axis, and $L$ and $D$ represent lift and drag forces, respectively. The angle of attack, $\alpha$, represents the angle of the flat plate relative to the freestream wind direction.

### 2.3.2 Moment Corrections

Due to the positioning of the plate in each assembly, corrections had to be made to compare the recorded experimental data to the model used by Chiappinelli and Nahon in [35]. In [35], the pitching moment is evaluated about the quarter-chord of the aircraft. However, in both the pitching and rolling setups, moments are measured about the centre of the force/torque sensor and the mounting rod, which is not aligned with the quarter chord, nor the body $y$-axis, of the acrylic flat plate. To account for this, in each case, a common point was used to compare the moments between the experimental data and the semi-empirical model.

#### Pitching Moment Correction

Consider the pitching moment setup, as seen in Figure 2.8. In this setup, the pitching moment $M_0$ is measured about the support rod, which is a distance $l$ behind the trailing edge of the acrylic model, defined by the length of the 3D-printed fixture. Meanwhile, the semi-empirical model from [35] provides the pitching moment about the quarter-chord point. Therefore, in order to compare the two values, the experimental moment about the quarter-chord of the acrylic model is calculated. As the body tangential forces pass through the longitudinal axis of the aircraft, they will not create any pitching moment about the quarter chord. Since the oncoming wind is assumed to have no velocity in the aircraft body $y$- direction, the normal body forces are the only forces to influence the pitching moment about the quarter-chord. The experimental pitching moment about the quarter-chord is calculated by,

$$\begin{aligned} M_{c/4} &= M_0 - N\left(\frac{3}{4}\bar{c} + l\right), \\ C_{M_{c/4}} &= \frac{2M_{c/4}}{\rho U^2 S\bar{c}}, \end{aligned} \tag{2.1}$$

where $N$ is the normal force to the plate at each angle of attack, $\bar{c}$ is the mean aerodynamic chord of the acrylic plate, and $\frac{3}{4}\bar{c} + l$ is the total distance from the rod to the quarter-chord of the flat plate. The pitching moment coefficient about the quarter-chord is denoted by $C_{M_{c/4}}$, the air density by $\rho$, the freestream velocity by $U$, the flat plate's surface area by $S$.

### Rolling Moment Correction

Consider the rolling moment setup, as shown in Figure 2.10. In the rolling moment setup, the mounting rod and force/torque sensor is aligned along the central axis of the acrylic model, and therefore records the rolling moment about the central axis $M_0$. For reasons that will be further discussed in Section 2.5.4, the semi-empirical model will return the rolling moment moment about the half-span on the port wing $M_{b/4}$, at point $p$ shown in Figure 2.10. In this case, both rolling moments will be considered along the body $x$-axis. Therefore, in the case of the semi-empirical model, the rolling moment about the body $x$-axis is calculated by,

$$\begin{aligned} M_0 &= M_{b/4} - N\left(\frac{b}{4}\right), \\ C_{M_0} &= \frac{2M_0}{\rho U^2 S b}, \end{aligned} \tag{2.2}$$

where $C_{M_0}$ denotes the rolling moment coefficient about the central axis, and $b$ denotes the span of the acrylic model.

### 2.3.3 Semi-Empirical Relationship

All experimental results are compared to an application of the semi-empirical relationship for thin rectangular plates at all angles of attack, presented in [36]. The semi-empirical model suggests that lift, drag, and pitching moment coefficients of a thin rectangular plate are functions of the plate's aspect ratio. In [35], this relationship is applied to the X-Vert tail-sitter by simplifying the body to nine rectangular strips, as shown in Figure 2.11. For example, in Figure 2.11(b), strips 2, 3 and 4 have flaps on their trailing edges, and strip 3 is set to be approximately the width of the propeller downwash, and will have a higher oncoming airspeed than other strips, due to propwash. Each strip is considered individually based on the windspeed passing over the section, and then the forces and moments applied to each strip are summed together. The application in [35] also adjusts the aerodynamic coefficients by considering effects from sweepback angle, and makes additional adjustments for flap deflections.

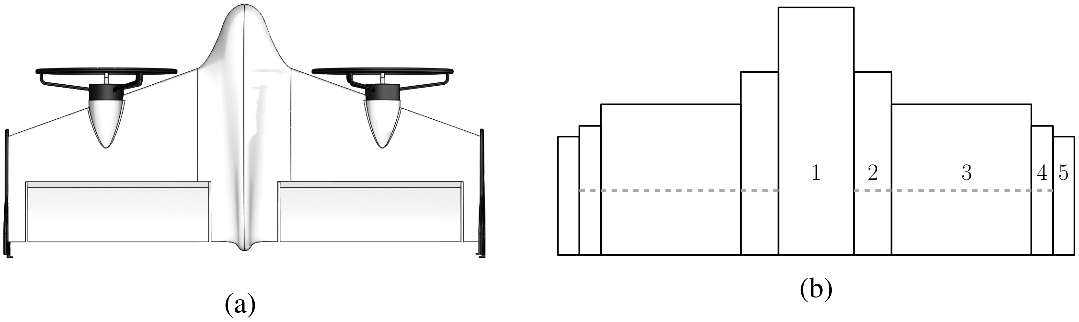

(a)
(b)

**Fig. 2.11**: a) Planform view of X-Vert tail-sitter. b) Planform view of simplified rectangular flat-plate model from [35].

### Implementation of the Semi-Empirical Model for the Pitching Setup

When considering the aircraft with oncoming winds at a specific pitch angle, the approach in [35] is used. In the present case, in order to compare to the experimental results, the method of [35] will be used with the same airspeed over every rectangular strip. The chord length for each rectangular strip is calculated by the average chord length of the X-Vert over the selected span, initially proposed by [35], and confirmed by 3D scanning the aircraft. In [35], each strip is then considered by the semi-empirical model. First, the oncoming wind vector is projected into the longitudinal plane of the flat plate, so that only the airspeed in the $x$- and $z$-directions in the aircraft's body frame are considered. For each rectangular strip, the approach in [35] considers the aspect ratio of the entire plate, $\text{Æ} = 3.2$, to generate the lift coefficient and drag coefficient, as well as the pitching moment coefficient about the quarter-chord. The lift and drag forces are assumed to be applied at the spanwise centre and the quarter-chord of each rectangular strip.

## 2.4 Pitching Rotation Experimental Results

The aerodynamic coefficient data at different pitch angles and Reynolds numbers is presented in Figure 2.12, Figure 2.13, and Figure 2.14. Aerodynamic coefficients are compared with those of [35], treating the aircraft as a sum of nine flat rectangular plates with an aspect ratio $\text{Æ} = 3.2$.

### 2.4.1 Lift Coefficient

The lift coefficient data is presented in Figure 2.12, showing that the lift coefficient generally collapses onto a single curve for all three Reynolds numbers, suggesting dynamic similarity at flight conditions. Since the acrylic flat plate model is symmetric, it follows that the lift coefficient curve follows the trend of an odd function about a $0°$ pitch angle. The method of [35] suggests a linear range of of $0° - 10°$, and, in this range, it predicts a lift curve slope of 3.7 rad$^{-1}$. When a line is fit to the experimental lift coefficient data in that range, the lift coefficient slope is 4.4 rad$^{-1}$, which is 20% higher. At this point, we do not have an explanation for the $20\%$ increase in lift curve slope.

This experimental data follows the same general shape and approximately follows the semi-empirical model proposed by [35]. This discrepancy in the flow separation angle — $10°$ predicted by [35], vs $12°$ indicated by the experiment — is reasonable for several reasons. First, the freestream turbulence level in the wind tunnel plays a major role in the angle at which flow separation begins. Hoffmann [40] showed that an increase in turbulence levels leads to an increase in flow separation angle on a finite wing section. However, they

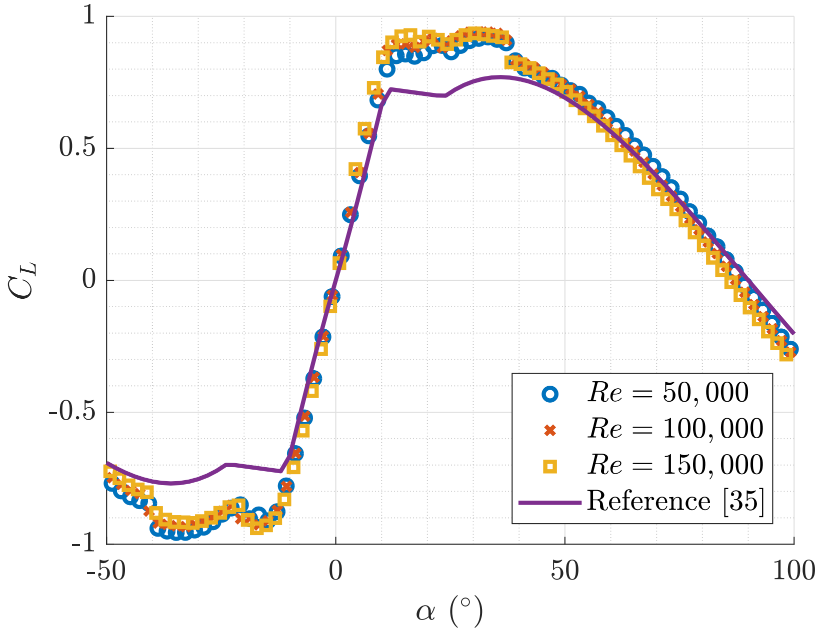

**Fig. 2.12**: Lift coefficient vs. pitch angle.

showed that the turbulence level has no significant effect on the lift curve slope. Thus, the delay of flow separation angle by about 2° may be due to the boundary layer and wake of the finite wing being energized by the background turbulence level in the wind tunnel of $1.1\%$ at a $10$ m/s freestream velocity.

The difference in the geometry of the flat plate could also account for the change in flow separation angle. The method of [35] determines the angle at which flow separation occurs by assuming the aircraft is a rectangular plate with no sweep. In both the real X-Vert tail-sitter and its flat-plate acrylic model, the leading edge of the tail-sitter has a sharp sweep angle near the root, followed by a lower, constant sweep angle along the wing. Furthermore, there are protrusions on either wing, due to the tail-sitter's motors. These can trip the leading edge vortices, and re-energize the boundary layer, potentially increasing the flow separation angle.

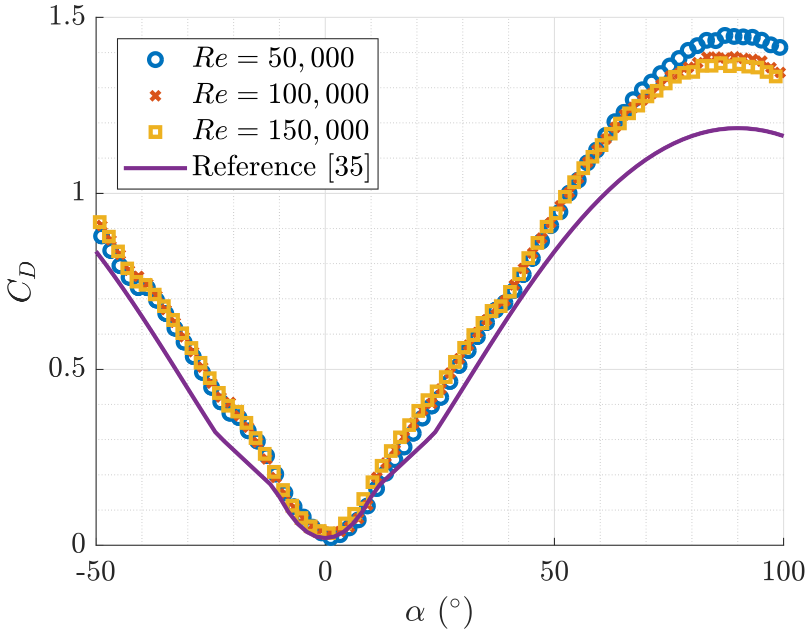

**Fig. 2.13**: Drag coefficient vs. pitch angle.

### 2.4.2 Drag Coefficient

The drag coefficient data is presented in Figure 2.13, and shows that the drag coefficients generally collapse into the same curve, again demonstrating dynamic similarity.

Since the acrylic flat plate model is symmetric, it follows that the drag coefficient curve follows the trend of an even function about a $0°$ pitch angle. This curve closely follows the modelled drag coefficient profile proposed by [35], with two minor exceptions. First, at a $0°$ angle of attack, the experimental flat plate drag coefficient is $C_D = 0.03$ which is double the predicted $C_D = 0.015$ by [35]. This result is reasonable, and can be accounted for by the thickness of the flat plate. The semi empirical model developed by Khan and Nahon [36] was based on plates with very low thickness-to-chord ratios, generally around $2\%$ [41], while the flat plate used in these experiments has a thickness-to-chord ratio of approximately $8\%$.

When the plate is nearly normal to the flow, around $90°$, the measured drag coefficient is higher than that predicted by [35]. This value is also higher than other published values.

Fail *et al.* [42] suggest that the drag coefficient of a flat rectangular plate with an aspect ratio between 2 and 5 normal to steady flow should be between $1.15$ and $1.22$, while our experimental model, with an aspect ratio of $\text{\AE} = 3.2$, has a drag coefficient around $1.35$. However, Humphries and Vincent [43] found that the drag coefficient of a circular disk normal to the flow could increase to $1.28$ as the turbulent flow intensity and integral length scale in the turbulent flow were increased. Similarly, Bearman [44] suggests that the drag coefficient of a flat plate normal to turbulent flow will increase on average by $8.6\%$ when the flow has $8.3\%$ freestream turbulence intensity. Thus, with some minor differences, we find that the lift and drag coefficients are adequately predicted by the method of [35].

### 2.4.3 Pitching Moment Coefficient

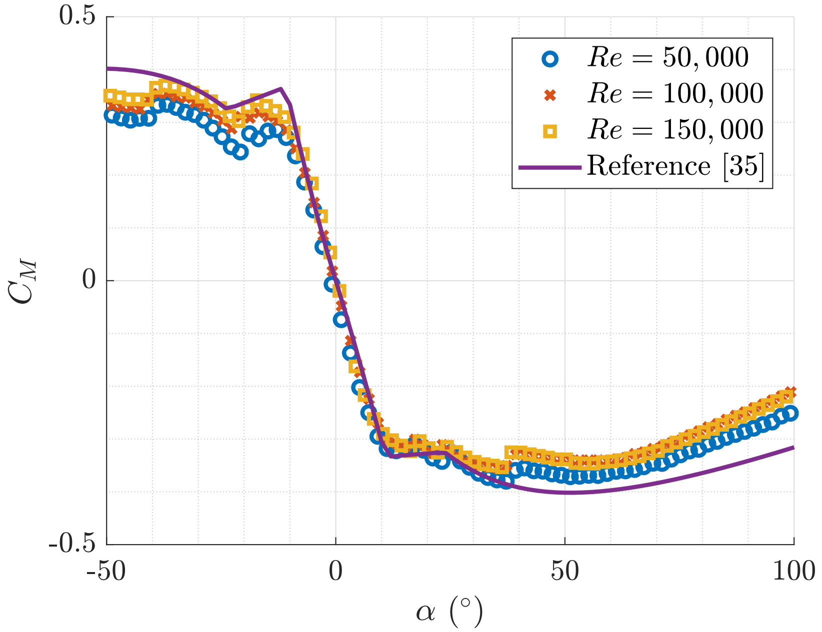

**Fig. 2.14**: Pitching moment coefficient vs. pitch angle.

The pitching moment data ia presented in Figure 2.14, and shows that, at low angles of attack, the quarter-chord pitching moment is consistent with [35]. However, differences become evident after flow separation occurs. This discrepancy may be due to the non-rectangular shape of the planform and different flow separation angle which can alter the pitching moment at a high angle of attack. This is further suggested by [41], which shows that the center of lift on a rectangular plate varies with aspect ratio as well as angle of attack. As there is evidence suggesting that both lift and drag coefficients are affected by higher freestream turbulence in the wind tunnel, it follows that the pitching moment coefficient may be influenced by this effect as well.

### 2.4.4 Additional Analysis

To summarize the data, we compare aerodynamic coefficients predicted by [35] to those measured in the three experimental runs. The data is separated into the linear region $(0°–10°)$, flow separation $(10° - 50°)$, and stall $(50°–90°)$. These values are defined by the model of [35], which estimates the flow separation angle and stall angle based on interpolation for existing data on rectangular flat plates with similar aspect ratios. The difference between experimental data and the model of [35] is shown in Table 2.4 in terms of normalized root-mean-square deviation (NRMSD),

$$\text{NRMSD} = \frac{1}{N}\sqrt{\sum_{i=1}^{N}\left(\frac{\hat{y}_i - y_i}{y_i}\right)^2} \times 100\%,$$

where $\hat{y}_i$ is the experimental value and $y_i$ is the value predicted by [35] over $N$ data points.

**Table 2.4**: NRMSD between aerodynamic coefficients from experimental data and from [35].

| | Linear | Flow Separation | Stall |
|---|---|---|---|
| $C_L$ | $17\%$ | $17\%$ | $6.7\%$ |
| $C_D$ | $17\%$ | $17\%$ | $14\%$ |
| $C_M$ | $10\%$ | $12\%$ | $21\%$ |

Consider the differences between the aerodynamic coefficients gathered experimentally and generated by the model in [35] in Table 2.4. Regarding the lift and drag coefficients, the model of [35] predicts values within $17\%$ of measured values. The NRMSD reduces further in the stall region, to $6.7\%$ and $14\%$ for lift and drag coefficients, respectively. Visually, in Figures 2.12 and 2.13, the difference in lift and drag coefficient appear mainly to be due to the higher angle of flow separation, which is likely a result of the higher turbulence level in the tunnel. The difference in the pitching moment coefficient predicted by [35] and measured those experimentally find a lower NRMSD in the linear and flow separation ranges, at $10\%$ and $12\%$, respectively, and has a higher difference in the stall region, with $21\%$ NRMSD.

**Table 2.5**: Correlation coefficient between aerodynamic coefficients from experimental data and from [35].

| | Linear | Flow Separation | Stall |
|---|---|---|---|
| $C_L$ | 1.000 | 0.998 | 1.000 |
| $C_D$ | 0.854 | 0.994 | 1.000 |
| $C_M$ | 0.998 | 0.998 | 0.998 |

The Pearson linear correlation coefficient between the experimental data and results from [35] are shown in Table 2.5. The Pearson correlation coefficient is calculated as,

$$r_{xy} = \frac{\Sigma_i (x_i - \bar{x})(y_i - \bar{y})}{\sqrt{\Sigma_i (x_i - \bar{x})^2}\sqrt{\Sigma_i (y_i - \bar{y})^2}}. \tag{2.3}$$

In this case, $x_i$ denotes an aerodynamic coefficient at one specific angle, measured experimentally and $y_i$ denotes the coefficient at the same angle, predicted by [35]. The main purpose of calculating the correlation coefficient is to determine the trends of the two data sets in a specific region; if both data sets increase with angle of attack, the correlation coefficient will be close to $r = 1$, whereas, over the range, if one data set increases while the other decreases, the correlation coefficient will approach $r = -1$. A correlation coefficient close to $r = 1$ is desired, as it suggests that both data sets have similar shapes, and may only have a difference in magnitude.

Although there are differences in amplitude, both the lift and pitching moment coefficients from experimental data and [35] are closely correlated, with correlation coefficients at or above 0.998 in all regions. The correlation coefficient in drag coefficient is lower, as low as 0.854 in the linear region, but is 0.994 in the region of flow separation, and 1.000 in the stall region.

### 2.4.5 Summary

The pitching model experimental tests suggests that the model of [35] is an acceptable approximation to model the variation of aircraft aerodynamics with angle of attack. For the lift, drag, and pitching moment coefficient, the experimental data collapses onto a single curve for all three tested Reynolds numbers. Therefore, it is safe to assume that the results for a full-scale aircraft would also collapse onto the same curve, implying that the semi-empirical model data can be used to predict the aerodynamic loads.

## 2.5 Rolling Rotation Experimental Results

The rolling rotation configuration shown in Figures 2.9 and 2.10 was considered next. The experimental aerodynamic coefficient data at different roll angles is compared to the values predicted by [35], shown in purple. A new proposed model, denoted by a green curve, will be further analyzed in Section 2.5.4. The resulting comparison is shown in Figure 2.15, Figure 2.16, and Figure 2.17.

### 2.5.1 Lift Coefficient

The lift coefficient data for the rolling experimental configuration (see Figure 2.9) is shown in Figure 2.15. The experimental data at the two different Reynolds numbers collapse onto the same curve once nondimensionalised, again suggesting dynamic similarity at flight conditions. The lift coefficient profile follows the general characteristics of a lift coefficient curve, in that it is an odd function about a $0°$ roll angle, and zero at both $0°$ and $90°$. The experimental values, however, deviate significantly from the results predicted by [35].

### 2.5.2 Drag Coefficient

The variation of the coefficient of drag with roll angle is whon in Figure 2.16. In this case, the work of [35] appears to approximately correspond with the trends of the experimental data, with strong differences in numerical results.

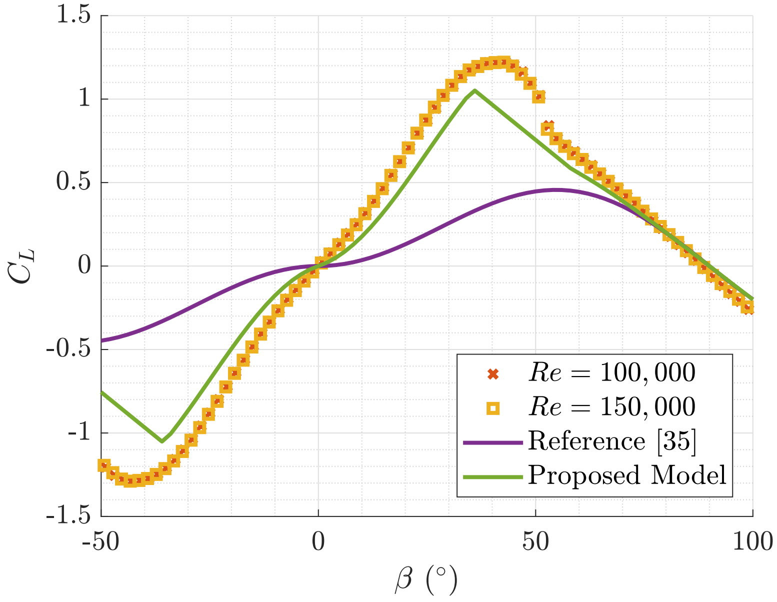

Fig. 2.15: Lift coefficient vs. roll angle.

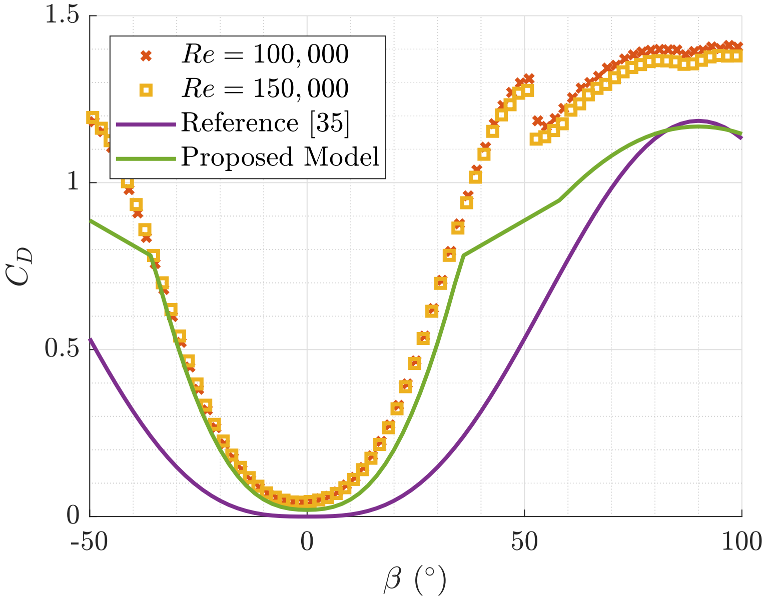

Fig. 2.16: Drag coefficient vs. roll angle.

### 2.5.3 Rolling Moment Coefficient

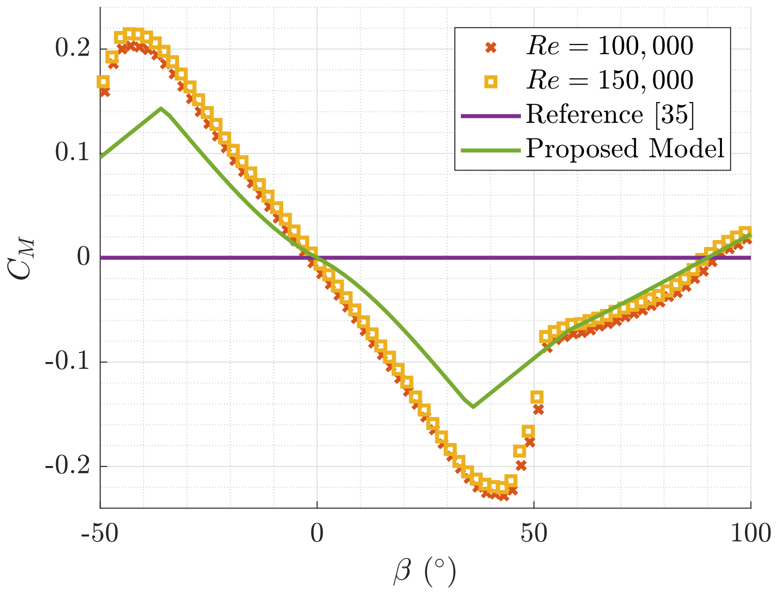

**Fig. 2.17**: Rolling moment coefficient vs. roll angle.

The rolling moment coefficient data is presented in Figure 2.17. Here, the flaws of the model used in [35] become striking, as that model predicts zero roll moment coefficient throughout the range.

### 2.5.4 Implementation of the Semi-Empirical Model for the Rolling Setup

Although the semi-empirical model from [35] can predict forces in the longitudinal plane and moments about the pitch axis, it cannot properly account for lateral airflow. In order to quantify this, the aerodynamic coefficients were investigated at various roll angles. By inspecting the aerodynamic coefficients as defined by the directions of lift and drag in Figure 2.10 returned by [35], we found that the results, shown in Figure 2.18 followed the form,

$$C_L = C_{D_{\max}} \frac{1}{2} \sin(2\beta) |\sin(\beta)| \tag{2.4}$$

$$C_D = C_{D_{\max}} |\sin(\beta)|^3, \tag{2.5}$$

where $C_{D_{\max}} = 1.185$ is the drag coefficient of a square flat plate normal to flow [44]. This drag coefficient has been found to be relatively consistent for rectangular plates with various aspect ratios [42], as well as for various shapes [45].

Although [35] models forces on the aircraft from lateral airflow, it assumes no rolling moment on the flat plate about the longitudinal axis. Since the set of rectangular strips are symmetric about the longitudinal plane, the lift distribution and drag distribution are symmetric about the longitudinal plane, and therefore generate no rolling moment about the longitudinal axis. This is incorrect, as, for example, a flat plate at a low angle of attack will have a centre of lift around its quarter-chord, and therefore a moment about its geometric centre.

We propose to apply the semi-empirical model by Khan and Nahon [36] to consider the aerodynamic forces and moments in the body $y$-$z$ plane, rather than the longitudinal $x$-$z$ plane. Consider Figure 2.19, which shows the tail-sitter subject to longitudinal and lateral winds, respectively. In Figure 2.19(a), the aircraft has a span $b = 50$ cm and a surface area $S = 776$ cm$^2$, and an aspect ratio $AR = \frac{b^2}{S} = 3.2$. However, in Figure 2.19(b), the "span", *i.e.*, the length of the plate perpendicular to the flow, can be considered to be $\bar{c} = 15.5$ cm, the mean aerodynamic chord of the aircraft, making the aspect ratio

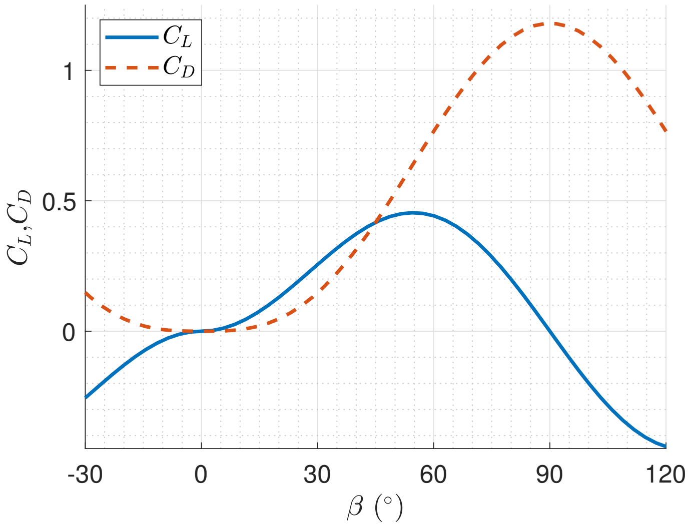

**Fig. 2.18**: Lift coefficient and drag coefficient vs. roll angle for lateral winds.

effectively $\text{Æ} = \frac{\bar{c}^2}{S} = 0.31$.

Therefore, while in the model of [35], the X-Vert aircraft is treated as a sum of nine rectangular segments with an overall aspect ratio $\text{Æ} = 3.2$, we propose that in the rolling case, we treat the aircraft as a single rectangular plate with an aspect ratio $\text{Æ} = 0.31$, as seen in Figure 2.20.

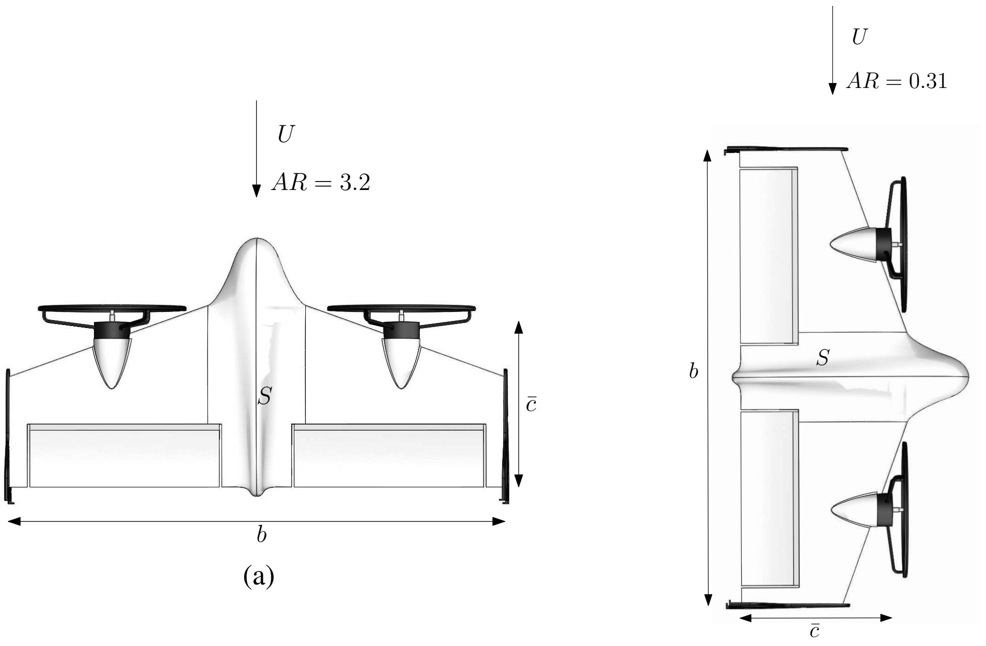

(a)

(b)

**Fig. 2.19**: a) Tail-sitter with oncoming flow in body $x$-$z$ plane. b) Tail-sitter with oncoming flow in body $y$-$z$ plane.

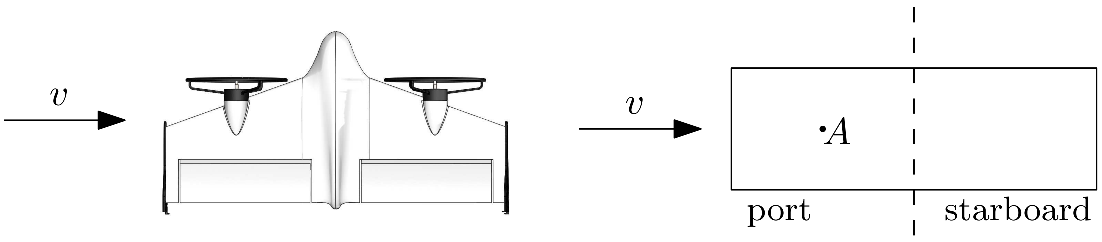

(a)

(b)

**Fig. 2.20**: a) Front view of hovering of X-Vert tail-sitter. b) Front view of simplified rectangular flat-plate model with aspect ratio $\text{Æ} = 0.31$.

Although simplifying the aircraft to a single rectangular plate may be an oversimplification of its geometry, it should serve as a first approximation of the aerodynamic forces and moments on a hovering X-Vert tail-sitter.

Due to the proposed application of the semi-empirical model of [36] for lateral airflow, the semi-empirical model will return a rolling moment about a point located one quarter of the distance between the leading edge and the trailing edge of the flat plate. In this case, we are considering that the flow passes across the entire span of the aircraft, and will, in the case of Figure 2.20(b), return the rolling moment about the half span of the port wing, shown as point $A$.

It should be noted that aerodynamic characteristics for rectangular plates with aspect ratios below $\text{Æ} = 0.5$ are much less common in literature, and as such, the semi-empirical model is less reliable for plates with such small aspect ratios.

### 2.5.5 Proposed model

Aerodynamic coefficients using the proposed model for a flat plate with aspect ratio $\text{Æ} = 0.31$ are denoted with a green line in Figure 2.15, Figure 2.16, and Figure 2.17. Visually, the proposed model returns values more consistent with experimental data than [35]. The proposed model predicts flow separation to occur at $\beta = 36°$, and stall at $\beta = 56°$.

#### Lift Coefficient

Returning to Figure 2.15, the proposed model matches relatively closely with experimental results, certainly better than the model from [35]. Although the proposed application predicts flow separation to occur at $\beta = 36°$, the experimental data suggests a delayed flow separation, closer to $\beta = 40°$.

As with the pitching case, the higher flow separation angle and maximum lift coefficient in experiment is likely a result of the higher freestream turbulence in the wind tunnel, as shown by [40]. Furthermore, the non-rectangular shape of the acrylic flat plate used in the experiments will likely affect the lift coefficient, in flow separation angle and maximum lift coefficient, as its different geometry affects the lift distribution over the plate.

According to the semi-empirical model, the linear range should cover $0° - 36°$, and, in this range, the lift coefficient slope is predicted to be 1.6 rad$^{-1}$. A linear fit to the experimental lift coefficient in that range indicates a lift coefficient slope of 1.9 rad$^{-1}$, which is 20% higher than the proposed model. This is consistent with data from the pitching setup, which suggests the difference may be a result of the experimental setup.

Generally, the proposed model, using an aspect ratio $\mathcal{R} = 0.31$ appears to match the experimental data substantially better than the model used in [35].

### Drag Coefficient

The proposed model, with an aspect ratio $\mathcal{R} = 0.31$ shows a reasonable match to the experimental data, especially before flow separation. As with the pitching test, the experimental drag coefficient for the bluff-body case, with the plate normal to flow is 1.35, as opposed to the theoretical value of 1.2, which is found by both the model from [35] and the proposed model with an aspect ratio $\mathcal{R} = 0.31$. This consistency across both the pitching and rolling setups is reassuring, and reinforces the idea that the increased drag coefficient is likely a function of the freestream turbulence in the wind tunnel and the experimental setup.

### Rolling Moment

The proposed model shows a much better fit to the trends of the experiment than the model used in [35]. While the proposed model underestimates the roll moment before flow separation, it provides and excellent match beyond $\beta = 50°$. Since the rolling moment about the central axis is a function of both the rolling moment about the middle of the port wing and the lift forces (see Eq. 2.2), the lower lift forces predicted by the proposed model may account for the lower rolling moment than the experimental values.

As with the other experimental data, roll moment indicates a higher angle of flow separation than the proposed model, likely accounted for by the freestream turbulence in the wind tunnel.

The roll moment predicted by the proposed model can also be used to infer the wing's stability at different roll angles. At roll angles of $0°$ and $90°$, where the roll moment is zero, the system is in an equilibrium state. However, the sign of the roll moment curve around these equilibrium points can be used to determine stability. In the neighbourhood of the first equilibrium point at $0°$, a small increase in roll angle results in a negative rolling moment, and a small decrease in roll angle results in a positive rolling moment — in both cases tending to oppose the disturbance. Therefore, this system is stable about the $0°$ equilibrium point. By contrast, in the neighbourhood of the $90°$ equilibrium point, a small increase in roll angle leads to a positive rolling moment, which will lead to larger roll angles. Therefore, the $90°$ roll orientation is an unstable equilibrium point.

This further stresses the need to plan a hovering tail-sitter to be aligned with the direction of oncoming wind. If a hovering tail-sitter is stable to small changes in roll when aligned with the wind, it will require less power consumption and smaller control surface deflections to stay aligned with the wind than a tail-sitter that is hovering while normal to the flow.

### 2.5.6 Additional Analysis

To summarize the data, the proposed model using an aspect ratio $\mathit{AR} = 0.31$ is compared to the average aerodynamic coefficients of the two experimental runs. The data is separated into the linear region $(0° - 36°)$, flow separation $(36° - 56°)$, and stall $(56° - 90°)$, as predicted by the proposed model.

**Table 2.6**: NRMSD between aerodynamic coefficients from experimental data and the proposed model.

| | Linear | Flow Separation | Stall |
|---|---|---|---|
| $C_L$ | 29% | 23% | 11% |
| $C_D$ | 30% | 26% | 19% |
| $C_M$ | 39% | 36% | 26% |

The proposed model of a rectangular plate with an aspect ratio $\mathit{AR} = 0.31$ appears to deviate further from experimental data for all roll angles than the model of [35] do in the pitching case. This could be because of the simplified rectangular model, which ignores the more complex planform geometry used in the wind tunnel tests. As with the pitching experiment, the difference between the model and the experimental data may be due to the background turbulence level in the wind tunnel, which likely delayed the flow separation angle of the experimental data.

With all aerodynamic coefficients, the proposed model returns high NRMSD in the linear regime, which reduces in the flow separation region, and further reduces in the stall region. For lift and drag coefficients, the NRMSD remains below 30%. The rolling moment maintains a NRMSD between $26\% - 39\%$.

Since the acrylic model is thick, non-rectangular, and subject to somewhat turbulent flows, and considering the lack of available data for flat plates with aspect ratios below $Æ = 0.5$, this is a promising first approximation.

**Table 2.7**: Correlation coefficient between aerodynamic coefficients from experimental and the proposed model.

| | Linear | Flow Separation | Stall |
|---|---|---|---|
| $C_L$ | 0.997 | 0.918 | 1.000 |
| $C_D$ | 0.990 | 0.583 | 0.983 |
| $C_M$ | 0.998 | 0.936 | 0.983 |

The Pearson linear correlation coefficient between the experimental data and the proposed model are shown in Table 2.5. Although results from the linear regime provide promising correlation coefficients, remaining at or above $0.990$. The stall region appears to provide some reasonable correlation, at or above $0.983$. However, in the flow separation range, there is little correlation between the two data sets. This may be a result of the difference between predicted and measured flow separation angle.

### 2.5.7 Sources of Difference

Although the acquired data provides a reasonable approximation for the aerodynamics of a cruising and a hovering flying-wing tail-sitter, there are some shortcomings associated with it. First, the experimental flat plate model does not account for airfoil features, such as the airfoil thickness and camber, or surface roughness. For example, at small angles of attack, the model of [35] predicted a lower drag coefficient than that measured experimentally, due to the acrylic model's higher thickness-to-chord ratio.

Furthermore, the experimental flat-plate model could not be used to validate the semi-empirical model's extensions, which include modelling the aerodynamics with flap deflections, or different wind speeds over different airfoil sections.

Nonetheless, this experimental setup did validate the semi-empirical flat plate model in situations in where the elevons are not deployed, and experiences uniform flow passing over it. This suggests that the semi-empirical model should provide a reasonable approximation of the aerodynamics of this aircraft, and is acceptable in a MATLAB Simulink framework to model the aircraft's flight.

# Chapter 3

# Wind Measurement and Estimation

In Chapter 4, we will develop a controller that requires knowledge of the instantaneous wind speed and direction relative to the aircraft. As mentioned in Section 1.3, there are no current methods to reliably estimate wind speed and direction relative to a flying fixed-wing aircraft. It is therefore of interest to develop a method that would allow measurement of relative wind speed and direction while hovering. Reference [24] was able to use six pairs of external pressure probes to determine oncoming wind speed and direction on a quadrotor. We will consider a similar approach to estimate wind speed and direction, that does not alter the aircraft geometry as significantly. In this chapter, a proof-of-concept study is conducted to ascertain if the wind speed and direction can be obtained from on-board pressure measurements.

For a flat plate normal to a flow, Bearman [44] found that the pressure difference between the upstream and downstream face of a plate decreases as the measurement point moves radially away from the centre of a square or circular flat plate. This effect is shown to be more pronounced in turbulent flow. Similarly, it is well-known that the lift distribution, and hence the pressure difference across the surface, over a three-dimensional lifting surface is not uniform, and varies with its angle of attack [38], as shown in Figure 3.1. Therefore, the pressure difference across a plate can be expected to vary at different locations depending on the oncoming wind speed and direction.

We hypothesize that this phenomenon can be used to estimate the oncoming wind speed

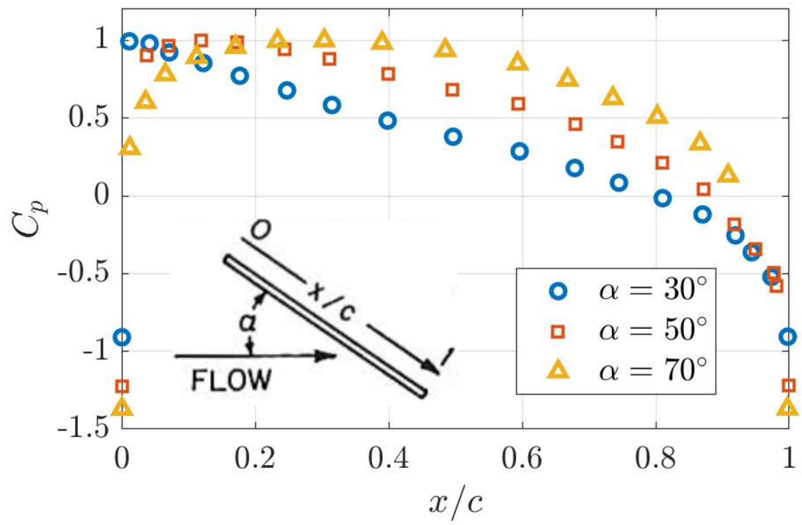

**Fig. 3.1**: Pressure coefficient distribution on an inclined flat plate [46].

and direction. Pressure taps embedded in a flat plate or airfoil can determine the local static pressure at that location. Ideally, we would like to determine the wind speed and direction based on the least possible number of measurements. Since most pressure transducers are differential, we would like to determine the wind speed and direction based on measuring the pressure difference between the two sides of the body, at multiple locations.

As a proof of concept, this will be tested by measuring the pressure difference across a plate with two pairs of pressure probes; one pair near the leading edge along the longitudinal axis, and one pair closer to the centre of the plate, as shown in Figure 3.2.

## 3.1 Experimental Setup

In order to measure the pressure difference across the flat-plate model, the vertically-oriented setup was used, as shown in Figures 2.9 and 2.10. A $1/16$" $\times$ $1/16$" slot was cut on both faces of the flat plate, aligned with the longitudinal axis. Both slots were fitted with a $1/16$"-diameter thin-walled aluminum tube, with a wall thickness of $0.005$", running the length of the flat plate model along its longitudinal axis (body $x$-axis). The gaps in the slot were filled with adhesive in order to create a flat surface.

Along the length of both tubes, $1/32$"- diameter holes were drilled to act as pressure taps; the first pair set 1.5 cm from the nose of the flat plate, and the second pair set 6 cm from the nose, near the plate's centroid, as shown in Figure 3.2 and Figure 3.3. Additional holes were drilled in the rod every 1.5 cm in case future pairs of holes are to be tested, as shown in Figure 3.4. For each experiment, all holes not in use were covered with tape. It should be noted that the second pair of holes considered, which are 6 cm from the nose, are intentionally not placed further back on the flat plate. If this methodology were implemented on the X-Vert tail-sitter, pressure probes nearer the leading edge are more likely to remain unaffected by propeller downwash, as shown in Figure 3.5.

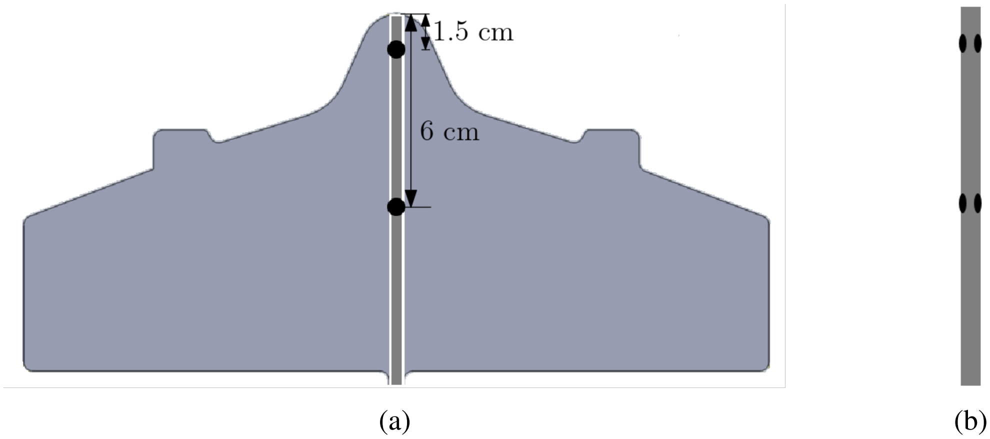

(a) (b)

**Fig. 3.2**: a) Sketch of front view of flat plate with embedded pressure taps. b) Sketch of side view of flat plate with embedded pressure taps.

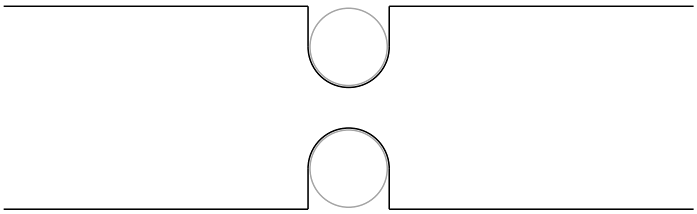

**Fig. 3.3**: Sketch of top view of flat plate with embedded tubing.

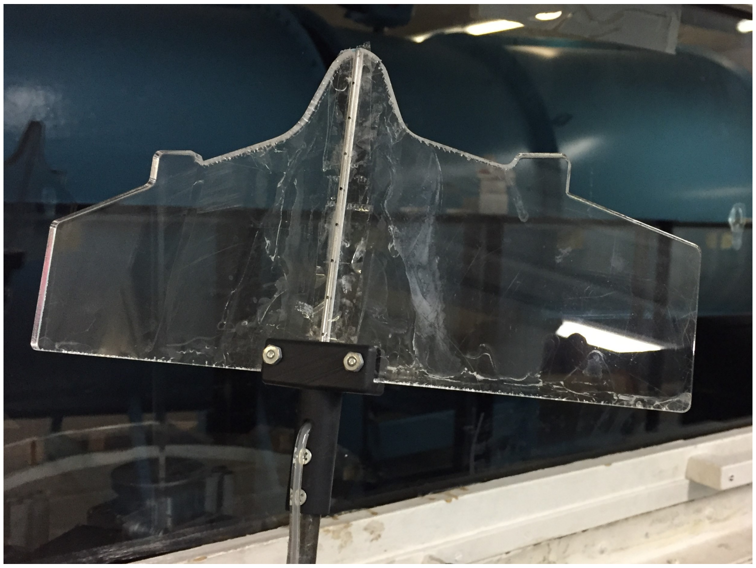

**Fig. 3.4**: Picture of flat plate with embedded tubing and pressure taps.

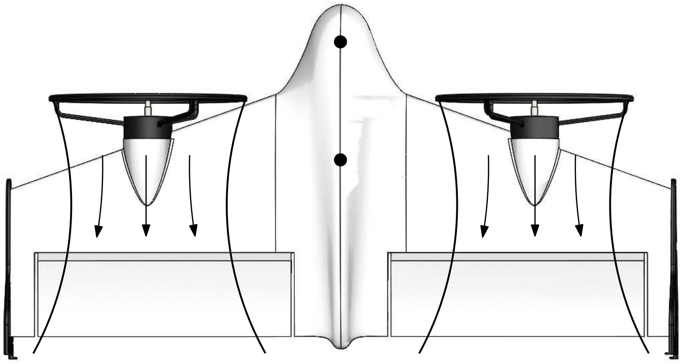

**Fig. 3.5**: Sketch of X-Vert tail-sitter with embedded pressure taps, and propeller downwash.

## 3.2 Experiment 1: Variation of pressure with roll angle

In order to understand the general relationship between wind velocity, direction and the pressure difference at both locations, measurements were first taken between roll angles of $-10° \leq \beta \leq 100°$ in $2°$ increments. Note that the pressure difference is defined as $\Delta P = P_{\text{front}} - P_{\text{back}}$. To represent Reynolds numbers ($\frac{Ul}{\nu}$) with the full-size tail-sitter hovering in wind speeds between $5$ and $10$ m/s, measurements for the half-scale model were taken at freestream velocities of $10$ m/s, $15$ m/s, and $20$ m/s. In order to confirm a roughly symmetric relationship, measurements at the $10$ m/s case were taken from $-10° \leq \beta \leq 200°$, once again in $2°$ increments. Each measurement was taken for $40$ s at a rate of $1000$ Hz, and averaged to find the mean pressure difference.

Figure 3.6 shows the recorded pressure difference across the plate near the nose (solid lines), and the pressure difference across the plate near the centre (dashed lines) at each wind speed. From Figure 3.6, the expected symmetry of the pressure distribution about $\beta = 90°$ is observed for the nose pressure tap at a freestream velocity of $10$ m/s. The remaining tests were therefore completed only for angles between $-10° \leq \beta \leq 100°$, to ensure that the $\beta = 0°$, *i.e.*, aligned with the flow, and $\beta = 90°$ *i.e.*, perpendicular to the flow, orientations were observed.

Some preliminary observations can be made for the presented data. For all experiments, around a roll angle of $55°$, there is a large spike in pressure difference across the plate. From the experimental data presented in Section 2.5, this coincides roughly with the roll angle at which flow separation begins for the flat plate. For angles less than $40°$, there is a small difference, roughly 2–4 Pa, between the differential pressure at the nose and the differential pressure at the centre. For angles greater than $40°$, the pressure difference using centre pressure taps is greater than the difference observed at the nose, with the difference between the two increasing as wind speed increases. Measurements about the centre tend to slightly increase in the post-stall region until the dip at $90°$, whereas the nose measurements tend to stay relatively constant until the dip.

The measured pressure differences were next non-dimensionalised and evaluated for all performed experiments. The pressure coefficient $C_p$ is defined as $C_p = 2\Delta P(\rho U^2)^{-1}$, where $\Delta P = P_{\text{front}} - P_{\text{back}}$ is the pressure difference between the upstream and downstream

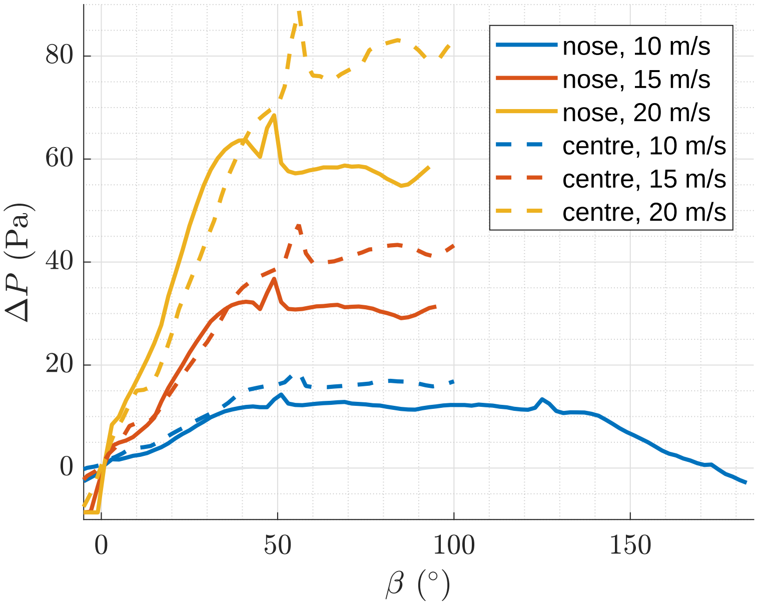

**Fig. 3.6**: Pressure difference across plate vs roll angle.

face of the plate at the desired location, $\rho$ is the air density, and $U$ is the freestream velocity. Results are shown in Figure 3.7. Although the results do not superimpose perfectly, there is a clear trend to the result. At angles beyond $\beta > 50°$, the pressure coefficient across the centre of the acrylic plate is larger than the pressure coefficient across the nose of the acrylic plate. Furthermore, the pressure coefficient tends to increase slightly as wind speed increases, suggesting that $C_p$ is not entirely independent of Reynolds number. Although one would hope to use a nondimensional value, like pressure coefficient, to deduce oncoming wind speed and direction, calculation of the pressure coefficient requires knowledge of the wind speed. Therefore, we will focus on the pressure difference at both locations to estimate wind speed and direction.

## 3.3 Experiment 2: Variation of pressure with wind speed

In order to get a clearer idea of the relationship between both differential pressure readings and the wind speed and direction, the experiment was repeated at additional wind speeds. As a general relationship was desired, the differential pressure was recorded at

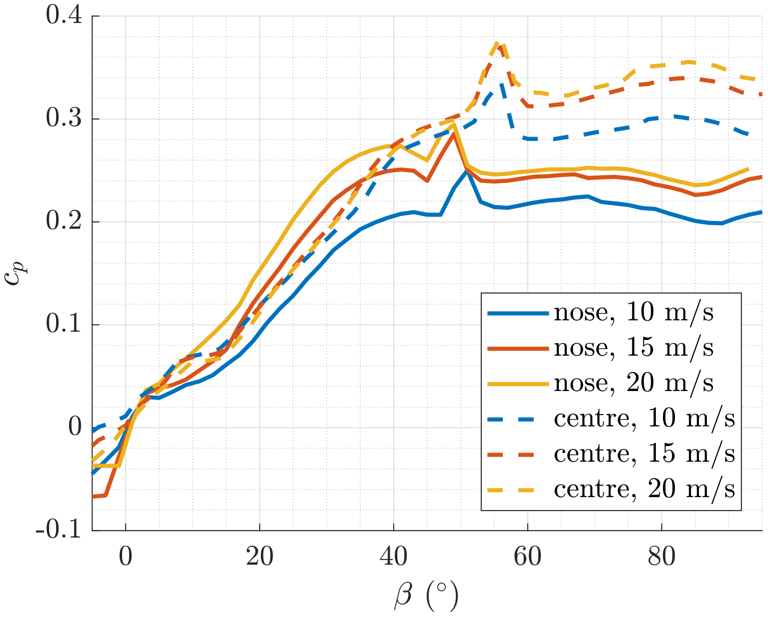

**Fig. 3.7**: Pressure coefficient across plate vs roll angle.

fewer roll angles, in 10° increments between $0° \leq \beta \leq 90°$ roll angles, for freestream velocities between 7.5 m/s and 20 m/s, in 2.5 m/s intervals. As with the Experiment 1, each measurement was taken for 40 s at a rate of 1000 Hz, and averaged.

By measuring the mean pressure difference 1.5 cm from the nose, and the mean pressure difference 6 cm from the nose, a general relationship between wind speed and direction and these pressure differences can be observed in Figure 3.8. Distinct curves distinguishing each orientation and each wind speed are observed for roll angles in the $40° \leq \beta \leq 90°$ range. For example, the data for roll angle $\beta$ appears to follow an approximately linear trend, with different slopes corresponding to each angle. Meanwhile, wind speed is approximately associated with $\Delta P_{\text{nose}}$; for a wind speed of 17.5 m/s, $40 \text{ Pa} \leq \Delta P_{\text{nose}} \leq 45 \text{ Pa}$, while for a wind speed of 20 m/s, $53 \text{ Pa} \leq \Delta P_{\text{nose}} \leq 62 \text{ Pa}$.

However, for roll angles $0° \leq \beta \leq 30°$, the pressure difference is smaller, and does not follow as clear of a trend.

The same data is shown in Figure 3.9, excluding pressure measurements at roll angles $0° \leq \beta \leq 30°$, as there were no discernible trends in this range from our current sensor.

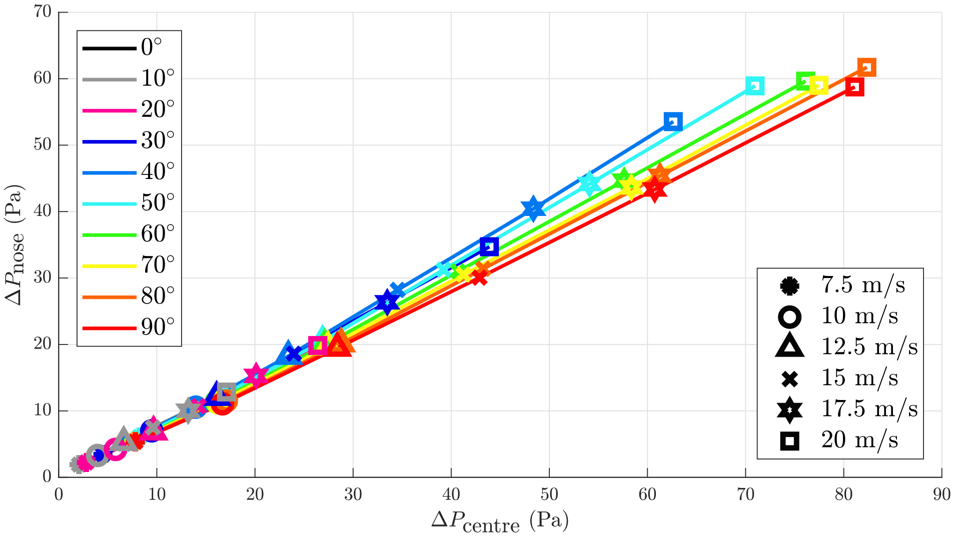

**Fig. 3.8**: Pressure difference at two points at wind speeds $7.5 - 20$ m/s, at roll angles $0° \leq \beta \leq 90°$.

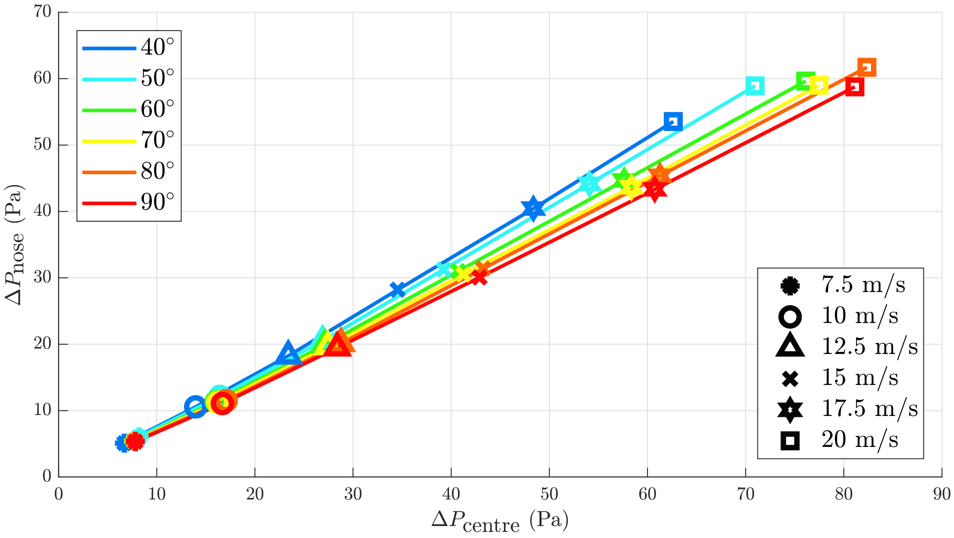

**Fig. 3.9**: Pressure difference at two points at wind speeds $7.5 - 20$ m/s, at roll angles $40° \leq \beta \leq 90°$.

With this information, it may be possible to infer wind speed and direction using these measurements.

## 3.4 Wind Prediction

The data measured in Experiment 1 in Section 3.2 suggests that there is a relationship between the oncoming wind speed and direction to the pressure difference measured on the body of the aircraft. The mapping between these variables is obtained by fitting a surface polynomial to the experimental pressure data, to find two individual functions, one for oncoming velocity and one for roll angle, as functions of the nose pressure difference and centre pressure difference. The coefficients of the surface polynomial were fit using least square regression with MATLAB function `lsqcurvefit`, using the pressure difference at both the nose and the centre positions, $\Delta P_{\text{nose}}$ and $\Delta P_{\text{centre}}$, respectively. Both pressure measurements were associated with seventy eight unique combinations of roll angles and freestream velocities, ranging from $40°$–$90°$ in $2°$ increments, and $10$–$20$ m/s, in $5$ m/s increments.

The surface polynomials were of the form:

$$\begin{aligned} U_{\text{est}} &= a_0 + a_1 \Delta P_{\text{nose}}^2 + a_2 \Delta P_{\text{nose}} + a_3 \Delta P_{\text{centre}}^2 + a_4 \Delta P_{\text{centre}} \\ &\quad + a_5 \Delta P_{\text{nose}} \Delta P_{\text{centre}} + a_6 \frac{\Delta P_{\text{nose}}}{\Delta P_{\text{centre}}} + a_7 \frac{\Delta P_{\text{centre}}}{\Delta P_{\text{nose}}}, \qquad (3.1) \\ \beta_{\text{est}} &= b_0 + b_1 \Delta P_{\text{nose}}^2 + b_2 \Delta P_{\text{nose}} + b_3 \Delta P_{\text{centre}}^2 + b_4 \Delta P_{\text{centre}} \\ &\quad + b_5 \Delta P_{\text{nose}} \Delta P_{\text{centre}} + b_6 \frac{\Delta P_{\text{nose}}}{\Delta P_{\text{centre}}} + b_7 \frac{\Delta P_{\text{centre}}}{\Delta P_{\text{nose}}}, \qquad (3.2) \end{aligned}$$

where $\Delta P_{\text{nose}}$ and $\Delta P_{\text{centre}}$ are measured in Pascals. The surface polynomial is set to a standard second order polynomial of two variables, with two additional terms. The ratio of nose-to-centre and centre-to-nose pressure difference are the final two terms in both Equations (3.1) and (3.2), and are added to increase the range of possible shapes achieved by the surface polynomial contours. The coefficients for each surface fit are presented in Table 3.1.

Once the surface polynomial fit was obtained using the data from Experiment 1, it was then tested on the data from Experiment 2. Contour lines of the polynomial fits of Experi-

**Table 3.1**: Surface polynomial coefficients for estimated wind velocity and angle.

| $a_i$ | | $b_i$ | |
|---|---|---|---|
| $a_0$ | $-1.6 \times 10^2$ | $b_0$ | $3.5 \times 10^2$ |
| $a_1$ | $-7.9 \times 10^{-3}$ | $b_1$ | $2.9 \times 10^{-1}$ |
| $a_2$ | $-5.3 \times 10^{-1}$ | $b_2$ | $1.3 \times 10^1$ |
| $a_3$ | $-9.2 \times 10^{-3}$ | $b_3$ | $2.7 \times 10^{-1}$ |
| $a_4$ | $6.6 \times 10^{-1}$ | $b_4$ | $-9.0 \times 10^0$ |
| $a_5$ | $1.7 \times 10^{-2}$ | $b_5$ | $-5.8 \times 10^{-1}$ |
| $a_6$ | $1.2 \times 10^2$ | $b_6$ | $-5.4 \times 10^2$ |
| $a_7$ | $5.8 \times 10^1$ | $b_7$ | $6.6 \times 10^1$ |

ment 1 are shown in Figure 3.10, along with the data from Experiment 2. The loop-shaped contour lines represent the surface polynomial contours for wind speeds, whereas the approximately parallel lines represent contours for wind direction. The plots are enlarged to show the predicted and measured pressures at $7.5$ m/s and $20$ m/s in Figure 3.11(a) and Figure 3.11(b), respectively.

In Figures 3.12 and 3.13, the estimated values for wind speed and roll angle are compared to the known speeds and orientations, respectively using error equations,

$$\begin{aligned} \text{Wind Speed Error } (\%) &= \frac{U_{\text{est}} - U_{\text{meas}}}{U_{\text{meas}}} \times 100\%, \\ \text{Direction Error} &= \beta_{\text{est}} - \beta_{\text{meas}}, \end{aligned}$$

where $U_{\text{est}}$ is the estimated wind speed from the surface polynomial, $U_{\text{meas}}$ is the measured freestream velocity, $\beta_{\text{est}}$ is the estimated relative wind roll angle, and $\beta_{\text{meas}}$ is the known relative roll angle.

The existing modified second order surface polynomial fit appears to estimate the wind speed accurately. Note that the calibration file, using data from Experiment 1, did not have any data for wind speeds below 10 m/s, and the test experienced its largest error for freestream velocities of 7.5 m/s, which was outside the range of the calibration data. The largest error for each known wind speed occurs at a roll angle of $40°$, at the bounds of the calibration data. For most measurements, the estimated wind speed error remains between $\pm 5\%$ of true values.

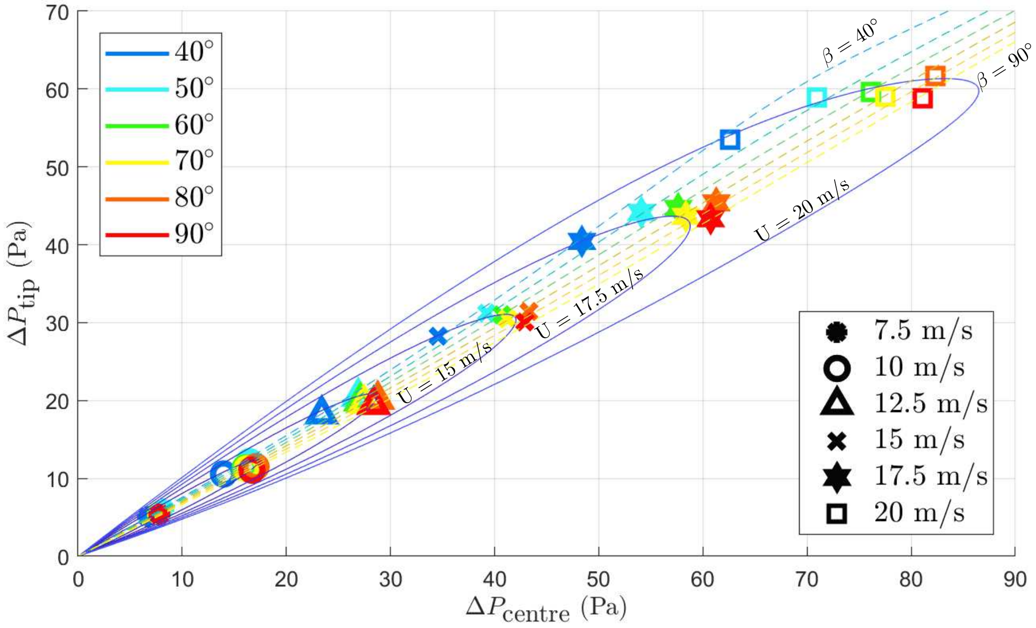

**Fig. 3.10**: Nose pressure difference vs centre pressure difference, showing roll angles between $40°$ and $90°$ and wind speeds between $7.5$–$20$ m/s. Dashed curves show predicted wind direction, in $10°$ increments, and solid curves show predicted wind velocity, in $2.5$ m/s increments.

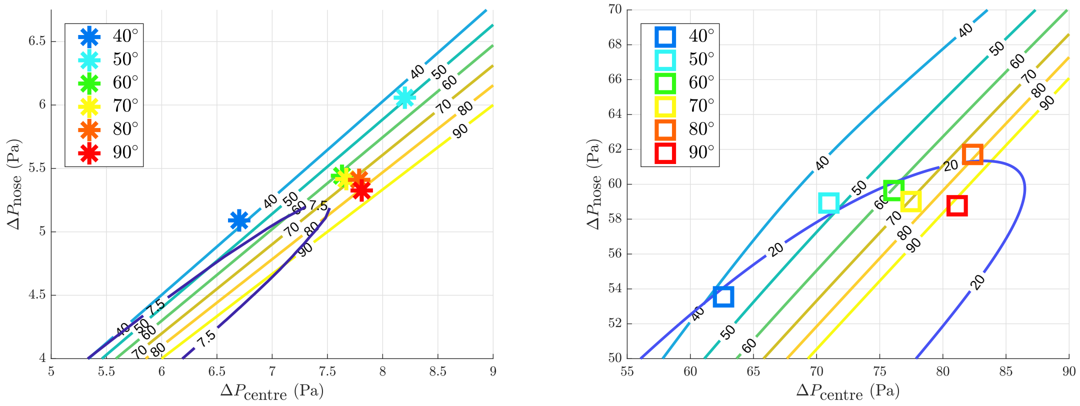

(a)

(b)

**Fig. 3.11**: a) Predicted and known values with v = 7.5 m/s b) Predicted and known values with v = 20 m/s. Contour lines show predicted values, and markers denote measured values.

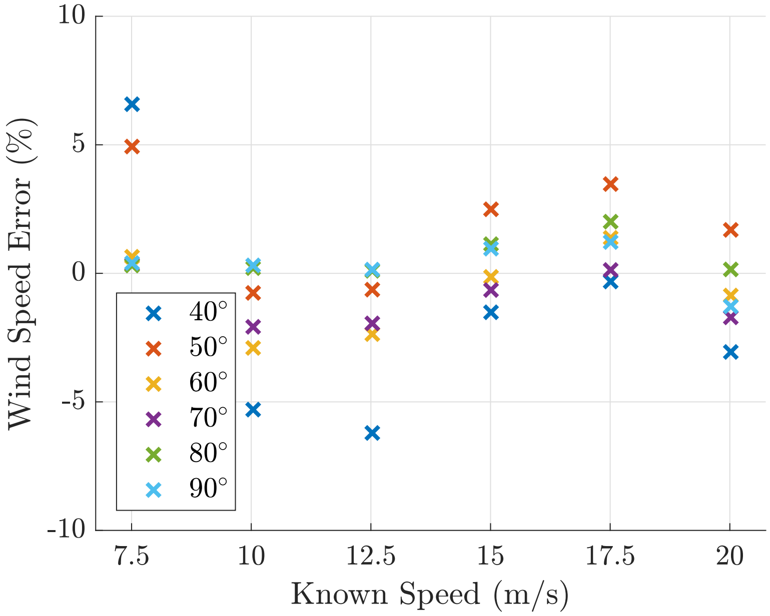

**Fig. 3.12**: Estimated wind speed % error vs known freestream velocity.

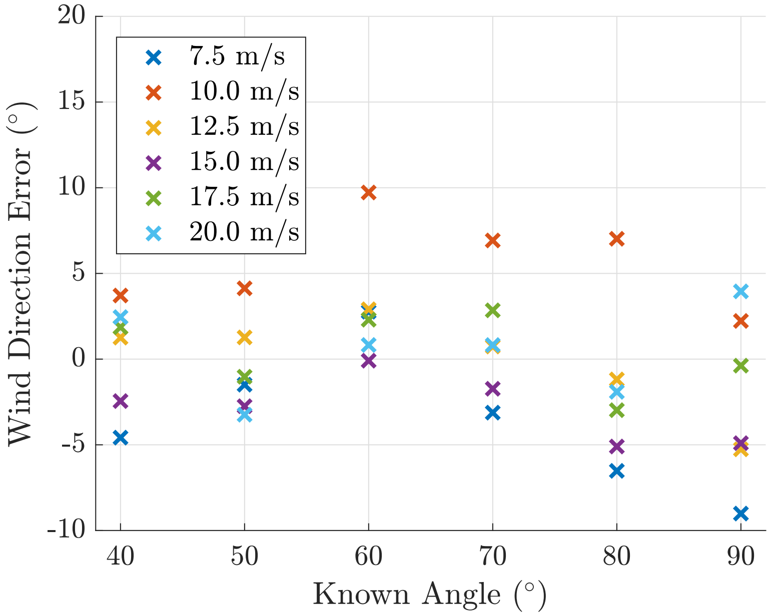

**Fig. 3.13**: Estimated roll angle relative error vs known roll angle.

The tested data for estimating wind direction returned estimates with a higher variance, of $10°$–$15°$, with individual measurements providing an error within $\pm 10°$ from the known roll angle.

Currently, in the limited range considered, the polynomial fits can be used to accurately estimate oncoming wind speed and direction. In real-world implementations, knowing the oncoming wind direction is vital in order to properly reject wind disturbances, for reasons that will be further discussed in Section 4.2.

### 3.4.1 Prediction Extensions

The existing methodology to predict oncoming wind speed and roll angle acts only as a proof of concept; in order to better estimate oncoming wind speed and direction, a larger data set, at more wind speeds and angles of attack, would be required.

The existing model fits the data to a second order polynomial, with two additional terms, as a function of the nose pressure difference and centre pressure difference. Although this provides a reasonable fit for determining wind speed, there is room to improve the fit for wind roll angle. By exploring other surface function fits, such as sinusoidal functions or higher order polynomials, it is possible that a more precise surface function fit can be determined.

This existing surface polynomial fit can also only estimate the oncoming wind speed and roll angle. In order to determine the oncoming wind speed and relative angle in all directions, considering roll, pitch and yaw, a minimum of four pairs of pressure taps would be required. With more pairs of pressure taps, a more precise model can be configured.

This existing model relies on the mean of pressure data that was recorded over $40$ s. In real-world applications, wind speed and direction can change drastically over the same period, and a mean reading may not return any useful data. In order to implement this on board an aircraft during flight, one would need to determine both wind speed and direction from a much shorter sampling time. This could be tested with an estimation framework to estimate the wind direction and velocity in real time.

## 3.5 Sources of Error

The experiments conducted in this section suggest that a relationship exists between the pressure difference at two points onboard an aircraft and the oncoming wind speed and direction. However, the results do not necessarily present an accurate model of the relationship on the UAV. This model assumes that all air passing over the aircraft has a low turbulence intensity $(1.1\%$ at $10$ m/s$)$. In outdoor situations, wind turbulence is regularly measured and modelled to be as high as $20\%$ [47–49], which may affect the pressure distribution over the plate. Nonetheless, these results suggest a relationship between the input of nose and base pressure differences and outputs of wind velocity and roll angle. With further work, such as placing additional pressure taps and gathering a larger data set, a more precise relationship between pressure tap reading and oncoming wind speed and direction can likely be determined to better estimate oncoming wind direction.

# Chapter 4

# Control Strategy

This chapter discusses the control strategies developed to control a tail-sitter aircraft in nose-up hovering flight. The goal was to improve upon the existing controller in [35], which had already been demonstrated to work well in other phases of flight, through feedforward control and improved orientation planning, to better reject wind disturbances. As such, we did not alter the controller gains used in [35].

## 4.1 Simulation Framework

The simulation framework and controller setup builds upon the work of Romain Chiappinelli, at the Aerospace Mechatronics Laboratory at McGill University [35]. As mentioned in Section 2.3.2, the aerodynamics model in the simulation considers the relative velocity of the wind to each individual strip of the aircraft geometry and determines the forces and moments acting on each strip. A block diagram of the overall Simulink model is shown in Figure 4.1. The aircraft model, shown in more detail in Figure 4.2, has as inputs the control deflections, and simulates the aircraft equations of motions, to produce aircraft pose. The controller block, shown in Figure 4.4, has inputs of wind velocity ($\mathbf{v}_{\text{wind}}$), and aircraft position ($\mathbf{p}$) and attitude ($\mathbf{q}$) and their temporal derivatives, from on-board sensors, and outputs desired control surface properties, notably elevon deflection $(\delta_l, \delta_r)$ and propeller throttle $(\tau_l, \tau_r)$ for both elevons and propellers.

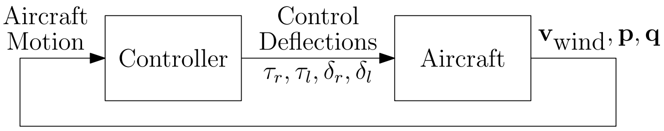

**Fig. 4.1**: Simplified block diagram of Simulink framework.

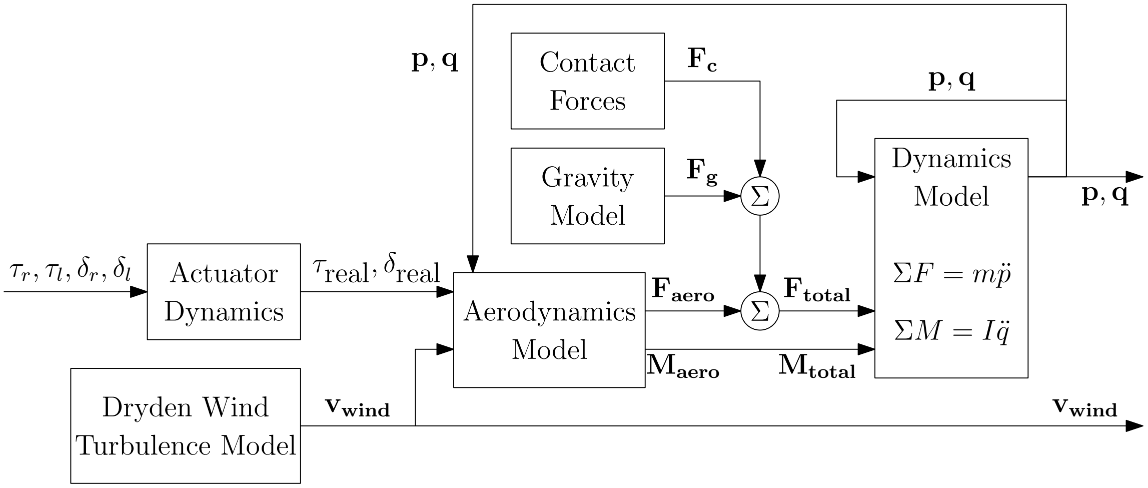

**Fig. 4.2**: Block diagram of aircraft model in Simulink framework.

A block diagram of the aircraft model is shown in Figure 4.2. This system calculates and sums the forces on the aircraft due to aerodynamics, gravity and ground contact, and applies them, as well as aerodynamic moments, to the aircraft equations of motion to evaluate translational and angular acceleration. These values are then integrated to evaluate velocities and pose. Further details of the model are found in [35].

### 4.1.1 Body-Fixed Reference Frame

Throughout this chapter, references will be made to the aircraft body-fixed reference frame, which are shown in Figure 4.3 for the X-Vert tail-sitter. This body-fixed reference frame is set about the aircraft's centre of mass. The body $x$-axis points towards the nose, the body $y$-axis points out its starboard wing, and the $z$-axis points out the bottom of the aircraft, such that all three axes are orthogonal. A rotation about the $x$-axis is considered a roll $(\phi)$, while pitch $(\theta)$ and yaw $(\psi)$ are used to define rotations about the $y$- and $z$-axes, respectively.

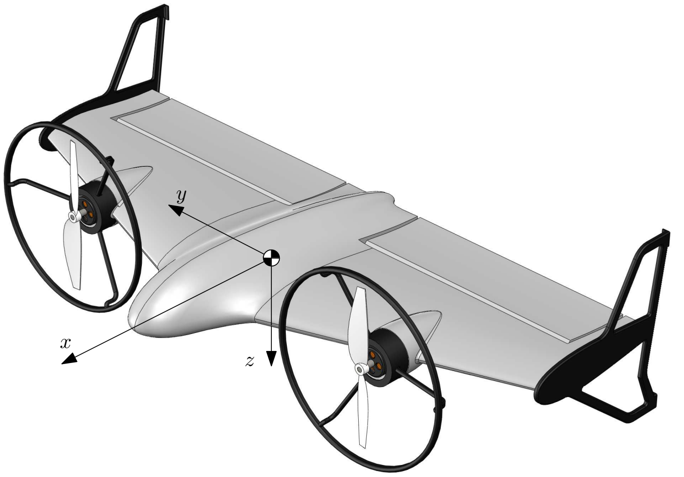

**Fig. 4.3**: Body-fixed reference frame of X-Vert tail-sitter.

### 4.1.2 Existing Controller

The existing work by Chiappinelli and Nahon [35] uses a cascaded quaternion controller, shown in Figure 4.4. The maneuver generator, provided with pose and forward velocity in the body frame, $u$, determines a user pre-defined reference pose $(\mathbf{p}_{\text{ref}}, \mathbf{q}_{\text{ref}})$ and forward velocity $(u_{\text{ref}})$, and outputs these values. The position controller considers the current and reference pose and, using a PID controller, calculates an orientation $(\mathbf{q}_{\text{des}})$ to reach such a pose. The desired orientation is provided to the attitude controller, which, using a PID controller, calculates the required moment $(\mathbf{M}_{\text{des}})$ to reach that orientation. Meanwhile, the thrust controller uses a PID controller to calculate the desired force $(\mathbf{F}_{\text{des}})$ required to reach the reference position. The desired forces and moments are combined in the actuator mixer, which calculates the control deflections required to provide appropriate forces and moments. Each controller has its own individually-tuned gains. In the simulation framework, it is currently assumed that the controller has perfect knowledge of all states, including aircraft position and orientation, as well as all temporal derivatives, such as translational and angular velocity, and wind speed and direction at each time step. The desired states are programmed into the maneuver generator before the simulation is run, and vary in time, depending on the desired flight path.

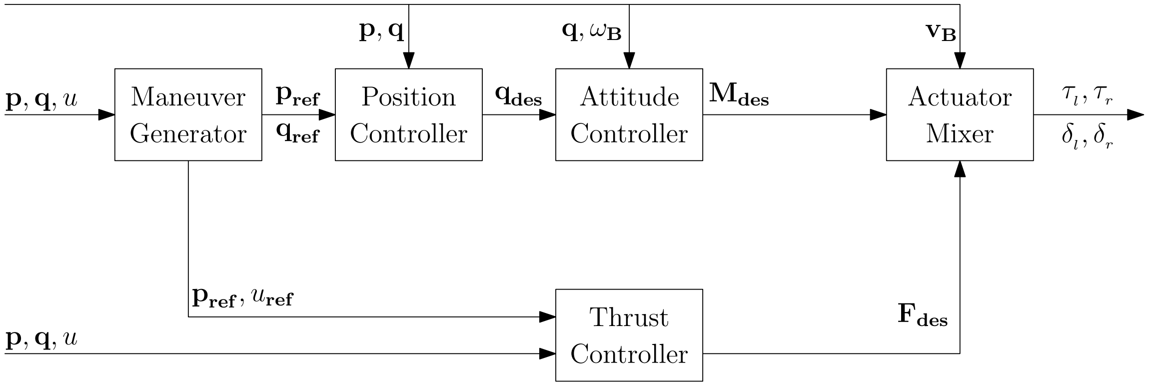

**Fig. 4.4**: Block diagram of cascaded quaternion-based controller.

### 4.1.3 Improvements to Simulation Framework

Although the proposed model for pure roll angles presented in Section 2.5.5 provides more precise results than the model of [35] for all aerodynamic coefficients, in the aircraft's $y$-$z$ body plane, implementing the proposed model is a complex task. The existing Simulink simulation considers relative airflows that can have any combination of angle of attack and sideslip angles. By contrast, the experiments performed in Section 2.5 only consider the case of a relative airflow that is always perpendicular to the aircraft's roll axis. It is not possible to easily merge the proposed roll model for cases of oblique flows, while simultaneously retaining the model of [35] for the pitching-related calculations.

Nonetheless, the aerodynamic force/moment model used in the simulation can be updated to incorporate an improved estimate of rolling moments.This is accomplished by considering the oncoming wind's component in the body $y$-$z$ plane, and using the improved model proposed in Section 2.5.5 for a flat plate with aspect ratio $\text{Æ} = 0.31$. From this, the normal force and rolling moment about the midpoint of the port wing are converted into a rolling moment about the body $x$-axis of the aircraft using Eq. (2.2). This moment is added to other moments and forces on the aircraft determined bthe existing aerodynamics model, and should improve the simulation of moments acting on the aircraft.

It should be noted that the simulation aerodynamic model is a model of the steady aerodynamics, and neglects unsteady forces or moments. As noted in [36], it is expected that the aircraft motions are slow enough and will not lead to unsteady aerodynamic effects.

### 4.1.4 Simulation Conditions

For all simulations, a simple flight profile was selected. In each case, the tail-sitter starts at rest $0.1$ m above the ground, to avoid ground contact forces as well as ground aerodynamic effects. The aircraft is commanded to rise vertically at a rate of $1.5$ m/s, to an altitude of $10$ m, where it hovers in a fixed position for the remainder of the simulation. The entire simulation lasts 60 s, and data is output in $5$ ms increments. This simulation requires initial conditions to be input for each run, with aircraft position, velocity and attitude. The simulation incorporates a Simulink block to implement a Dryden Turbulence Model. A sample wind profile with an average wind speed of 2 m/s North $(0°)$, at an altitude of $h = 10$ m generated by this Simulink block is provided in Figure 4.5. The chosen flight path, *i.e.*, take-off and hover, along with the chosen flight time, were specifically chosen as they represent the conditions under which the aircraft is most susceptible to wind gusts. Landings were not evaluated, as its controllers appeared to struggle with vertical landing when subject to strong winds. This was mainly an issue with the existing controller not being designed for commands in the direction of the negative $x$-axis in the body frame. The controllers struggled with aircraft orientation when flying backwards, and would occasionally try to descend with a nose-down orientation, which would result in a crash landing, rather than a safe descent.

### 4.1.5 Evaluation Criteria

In each simulation, a specific criterion had to be met in order for the flight to be considered successful. The main metric used was the Root Mean Square Error (RMSE) of the UAV position over time. If the RMSE of the aircraft position over the 60 second flight simulation was larger than the mean aerodynamic chord $(\bar{c} = 7.76 \text{ cm})$, the flight was considered unsuccessful, as the aircraft was unable to stay close enough to the given reference position, on average, over the duration of the simulation.

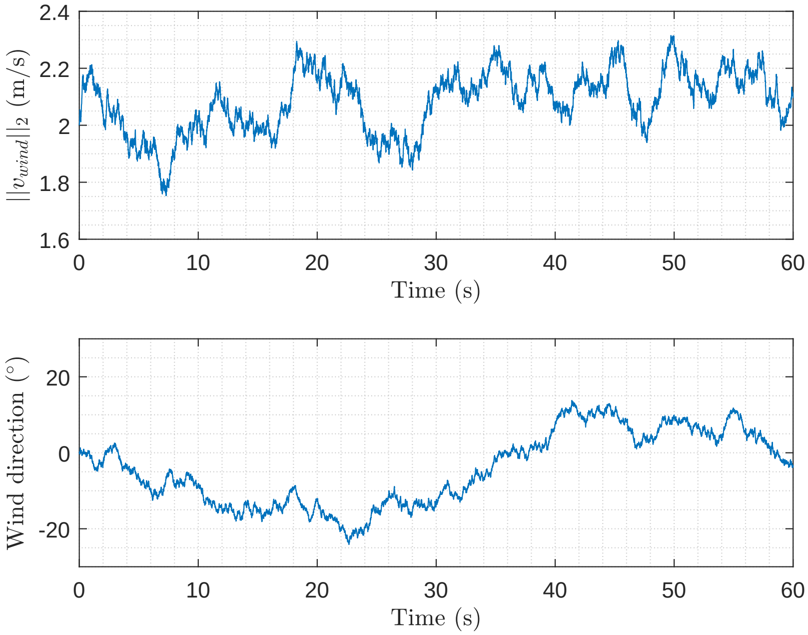

**Fig. 4.5**: Sample wind profile in a Northerly direction with 2 m/s mean velocity, obtained from MATLAB Simulink Dryden Wind Turbulence Model.

## 4.2 Feedforward Compensator

The first idea evaluated for improved control in windy conditions was to introduce feedforward control to the controller architecture. A feedforward controller is based on the idea that if the disturbance force and moment on the system is known, we can directly use the available actuation to cancel them. In a fully actuated system, with no delays or saturation, there will be zero position and attitude error if feedback and feedforward control are used together. However, the X-Vert tail-sitter is an underactuated system, as its control surfaces cannot apply forces in the body $y$-axis direction. Furthermore, the modelled tail-sitter considers that there are maximum deflections and deflection rates for the control surfaces, such as elevons. Finally, sensor noise prevents controllers from knowing exact oncoming force and moment disturbances.

### 4.2.1 Implementation of Feedforward Compensator

The existing controller architecture is set up in a way which facilitates the feedforward of forces and moments to the system. Although not shown explicitly in Figure 4.4, the Thrust Controller block does have some feedforward compensation to counteract gravitational forces. Within that block, the gravity force is calculated and an additional thrust is commanded to counteract it.

In this section, we introduce a feedforward compensator for aerodynamic forces and moments acting on the aircraft. The Feedforward Compensator block, shown in Figure 4.6, is essentially identical to the Aerodynamics Model shown in Figure 4.2. Given the aircraft position and orientation, and their respective temporal derivatives, as well as control surface deflections and wind speed, the Feedforward Compensator calculates the expected aerodynamic forces and moments acting on the aircraft. Thus, $\mathbf{F}_{\text{aero}}$ and $\mathbf{M}_{\text{aero}}$ shown in Figure 4.6 will be the true aerodynamic forces and moments, and will lead to perfect tracking if the motion variables are accurately measured and the Aerodynamics Model is perfect. Both these are flawed assumptions, due to sensor and model uncertainty, but those flaws will not be considered here.

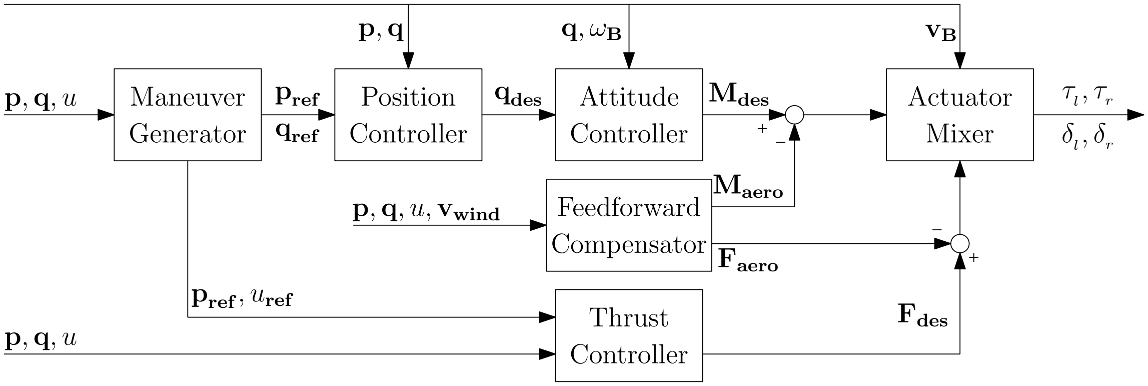

**Fig. 4.6**: Block diagram of cascaded quaternion-based controller with added feedforward compensator.

With the addition of the feedforward compensator, the forces and moments sent to the actuator mixer, $\mathbf{F_{act}}$ and $\mathbf{M_{act}}$, respectively, are,

$$\begin{aligned}\mathbf{F_{act}} &= \mathbf{F_{des}} - \mathbf{F_{aero}},\\ \mathbf{M_{act}} &= \mathbf{M_{des}} - \mathbf{M_{aero}},\end{aligned}$$

where $\mathbf{F_{des}}$ is the desired force output by the Thrust Controller, $\mathbf{M_{des}}$ is the desired moment output by the Attitude Controller, and $\mathbf{F_{aero}}$ and $\mathbf{M_{aero}}$ are the aerodynamic forces and moments, respectively, calculated by the feedforward compensator.

### 4.2.2 Simulation Overview

The simulation, in which the aircraft takes off and hovers with unsteady winds, was executed in two scenarios. First, the original controller was tested, then the same controller with feedforward control added was evaluated. In both cases, the tail-sitter takes off and hovers with its planform normal to the flow. As such, forces in the body $y$-direction are negligible, and forces in the body $x$-direction are small, as most wind forces on the aircraft are in the body $z$-direction. Similarly, rolling and yawing moments from the wind passing over the vertically-oriented aircraft are small, but pitching moments are significant. In both simulations, the aircraft attempts to maintain a constant attitude, with its body $z$-axis aligned with the initial wind direction, throughout the experiment, meaning the tail-sitter tries to stabilize about its unsteady equilibrium orientation, found in Section 2.5.5.

### 4.2.3 Simulation Results

A sample time series of the position with feedforward control is shown in Figure 4.7, in which the aircraft is flying under 2 m/s unsteady winds without feedforward control. The aircraft reaches the desired altitude around $t = 8$ s, then attempts to hover in a constant position for the remainder of the simulation. The largest peak in position error occurs in the first few seconds, as the aircraft is taking off. While taking off, the tail-sitter's vertical velocity is on the order of the wind velocity. Therefore, the aerodynamic forces caused by the wind passing over the aircraft cause a large deviation from the desired trajectory. The position error reduces as the aircraft continues to ascend, and is at its lowest when the tail-sitter hovers at a nominally fixed location. For these reasons, adjusting the hovering altitude or the hovering time should have a negligible effect on the error profiles, and this comparative study should be valid regardless of hovering height or hover time.

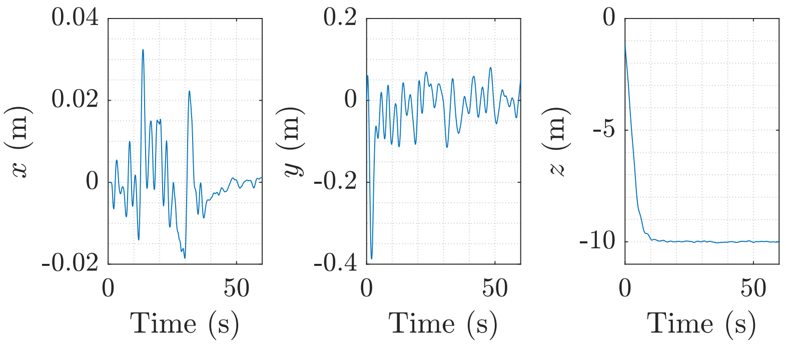

**Fig. 4.7**: Position of aircraft flying with 2 m/s wind.

The position error for the simulation with a wind speed of 2 m/s is shown in Figure 4.8. At this wind speed, the aircraft still has an acceptable performance, as its position RMSE is less than one mean aerodynamic chord length. It's inertial $x$-direction position error is small, which is reasonable, given the fact that the wind generally passes in the inertial $y$-

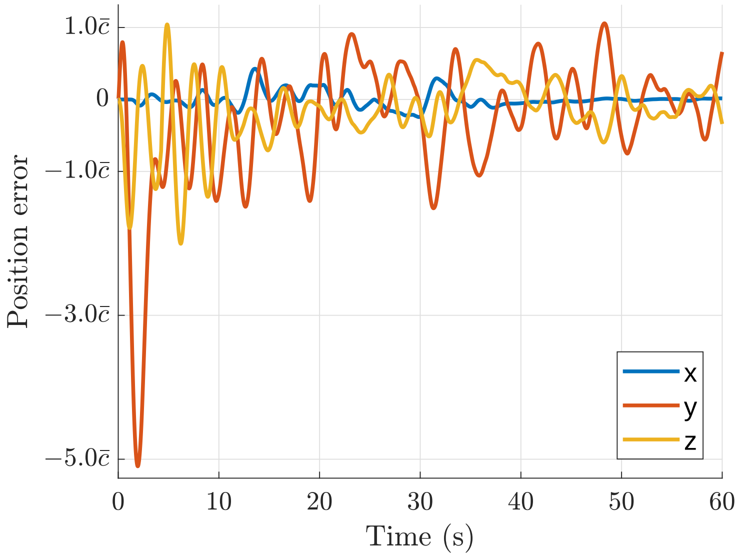

**Fig. 4.8**: Position error in inertial $x$, $y$ and $z$ directions, with 2 m/s wind speed.

direction, excluding fluctuations. However, the $y$-position error, in the same direction as the wind, the aircraft has its most significant position error on take-off, which results in the position RMSE increasing. During this flight path, the elevons have high deflections, but are not yet saturated, as seen in Figure 4.9. Snapshots of the tail-sitter flying are seen in Figure 4.10.

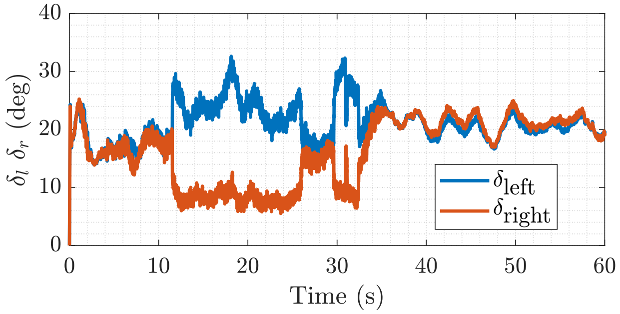

**Fig. 4.9**: Elevon deflections with $2.0$ m/s mean wind.

Positional error of the aircraft with and without feedforward control with $2$ m/s mean wind speed is shown in Figure 4.11. Although the feedforward compensator reduces position error on take-off, it provides only a small improvement in position error while hovering.

In Figure 4.11, it can be seen that, as expected, the addition of feeedforward control to the existing control architecture reduces position error throughout the simulation. Specifically, the feedforward controller has the most significant benefit on tak-eoff, as it reduces the transient position error due to drag forces, which moves the aircraft away from the reference position. Furthermore, the feedforward controller counteracts the pitching moment of the wind acting on the aircraft.

After the single simulation with an initial wind speed of $2$ m/s, the simulation was repeated for a range of wind speeds, all perpendicular to the aircraft, *i.e.*, nominally aligned with the body $z$-axis. Results are shown in Figure 4.12.

Although the addition of feedforward control reduces the position RMSE at each wind speed, it does not have a significant effect on the maximum wind speed that the tail-sitter can handle before its RMSE exceeds one mean chord length. This is a result of the control surfaces being saturated. An example of elevon deflections will be shown in Section 4.2.4.

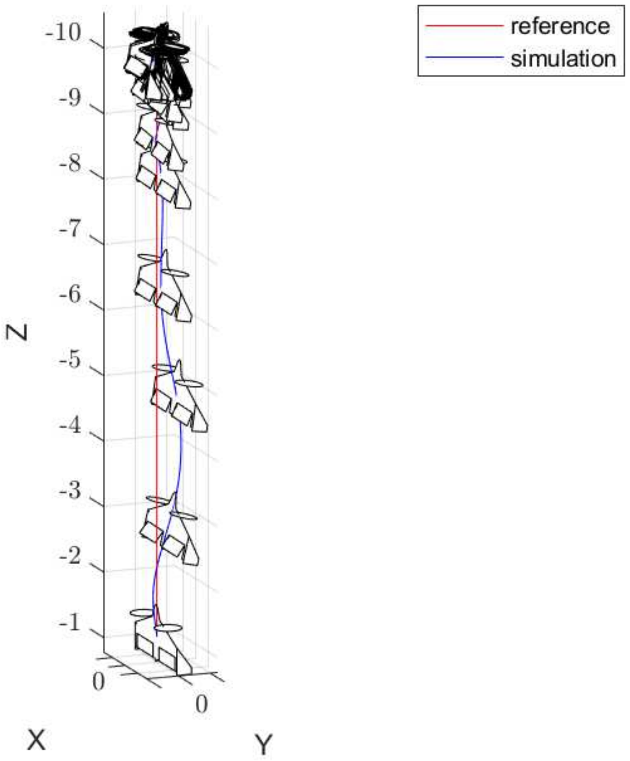

**Fig. 4.10**: Flight profile of aircraft flying with 2 m/s winds. Snapshots of position and attitude are taken every 1 s.

Under strong winds, there is a strong drag force, moving the aircraft away from its desired position, and a strong pitching moment on the aircraft. Even with both elevons at their maximum deflection angle, the aircraft cannot provide a strong enough moment to counteract the pitching moment from the wind. It follows that the addition of feedforward control cannot increase the range of wind speeds at which the aircraft can perform satisfactorily when normal to the wind; at high wind speeds, the control surfaces are saturated and cannot provide the moments commanded by the controller. In this section, the addition of feedforward control assumes that the controller have perfect knowledge of oncoming wind speed and direction. As shown in [26], sensors will generally have noisy outputs, and not have exact knowledge of wind properties. With less precise knowledge of the oncoming wind velocity, the feedforward controllers will be even less effective at reducing position error. Therefore, in order to reduce the effect of oncoming wind disturbances, other op-

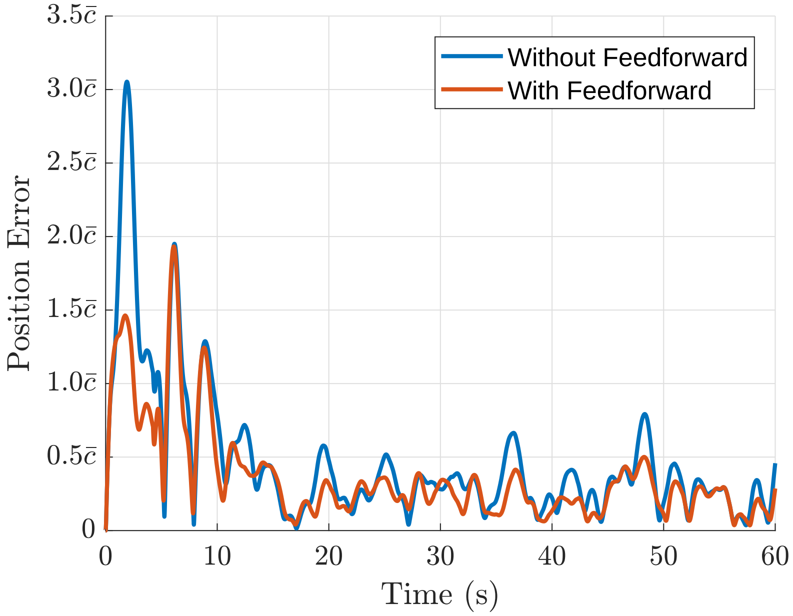

**Fig. 4.11**: $\mathcal{L}_2$-norm of tail-sitter position error through take-off and hover normal to wind vs time, without and with feedforward control, with a mean wind speed of 2 m/s.

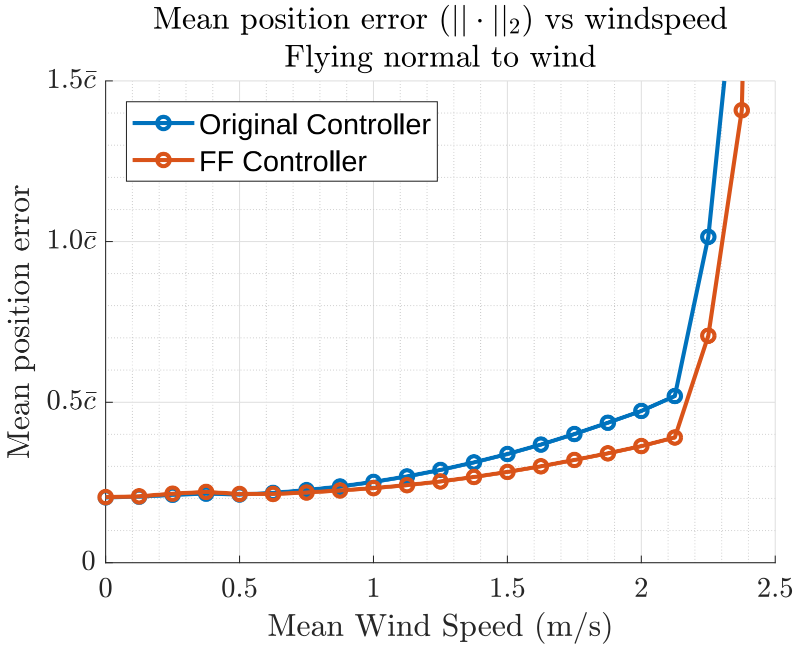

**Fig. 4.12**: RMSE of tail-sitter position error through take-off and hover, without and with feedforward control, vs initial wind speed.

tions besides the addition of feedforward control should be considered. In future sections, to evaluate other wind disturbance rejection methods, the feedforward compensator will not be used.

### 4.2.4 Additional Information - Simulations of Interest

To further display the results presented in Section 4.2.3, details of three simulations of interest were taken at two more wind speeds of interest: $0$ m/s and $2.5$ m/s. In Figure 4.12, there is a non-zero RMS position error, even at zero wind speeds. The RMS position error is approximately $0.2\bar{c}$, which is a result of the aircraft flight path. The desired flight path moves in a vertical path at a speed of 1.5 m/s, until it approaches the desired hover path, where it decreases to 0 m/s. Consider the position error for the simulation with zero wind speed, shown in Figure 4.13. On a windless take-off, the aircraft lags below the desired position, in the inertial frame, and eventually asymptotes towards the proper altitude, while the horizontal positional errors, in the inertial $x - y$ plane, are negligible.

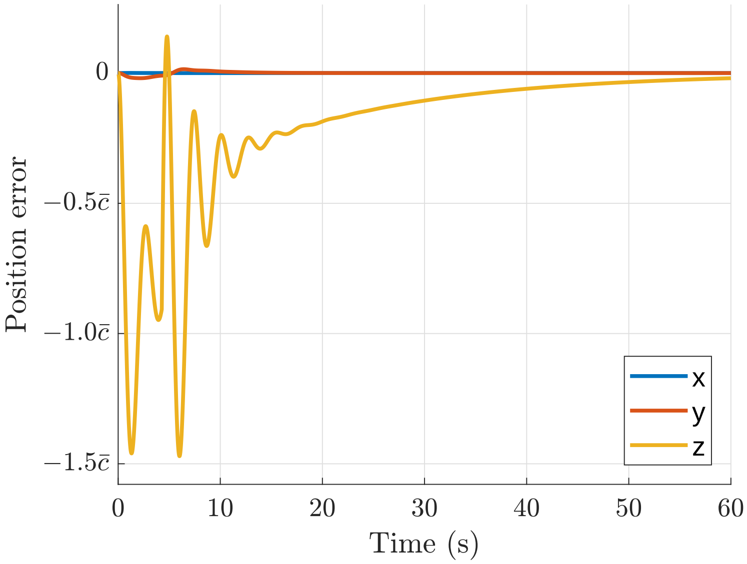

**Fig. 4.13**: Position error in inertial $x$, $y$ and $z$ directions, with $0$ m/s wind speed.

Consider the position error for the simulation with a wind speed of $2.5$ m/s, shown in Figure 4.14. Under the stronger wind conditions, the position RMSE significantly exceeds one mean aerodynamic chord length. On its ascent, the aircraft deviates several chord lengths away due to the wind, but it readjusts to its desired trajectory. However, $34$ s into the simulation, while hovering, a strong wind gust destabilized the aircraft, causing it to deviate from its desired position. At this point, the aircraft did not have the control authority to return to its desired position, as its elevons, shown in Figure 4.15, were at their maximum deflection and could not provide any stronger moment, and the tail-sitter crashed into the ground approximately 30 m away from its desired position.

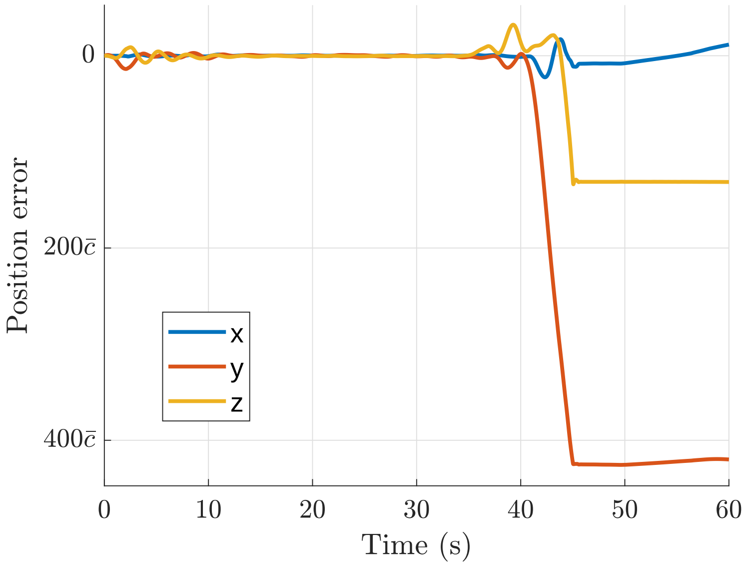

**Fig. 4.14**: Position error in inertial $x$, $y$ and $z$ directions, with $2.5$ m/s wind speed.

## 4.3 Orientation Planning - Fixed Orientations

After flying the aircraft at a fixed orientation normal to the wind with and without feedforward control, we next tested taking off and hovering in different orientations relative to the oncoming wind direction. The simulation of Section 4.2.3 was repeated with the aircraft starting aligned with the oncoming wind direction, and attempting to maintain that orientation.

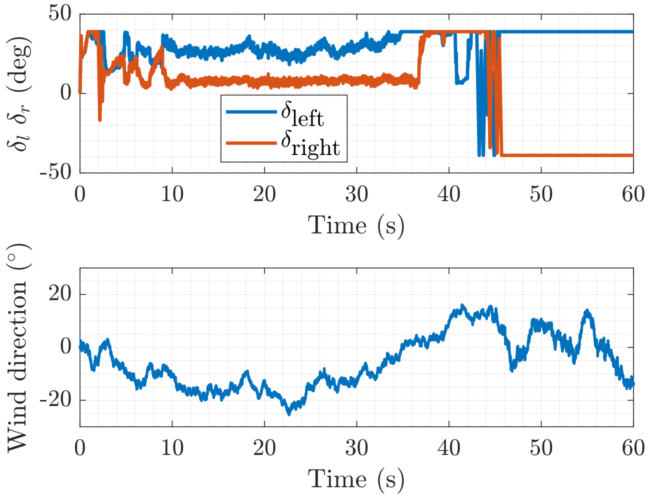

**Fig. 4.15**: Elevon deflections and wind direction for aircraft subject to 2.5 m/s mean wind speed.

### 4.3.1 Simulation Results

Results of the two are compared in Figure 4.17. As suggested on the X-Vert packaging, flying aligned with the oncoming wind direction does increase the maximum wind speed in which the aircraft can fly. In this case, flying aligned with the original wind direction nearly doubled the mean wind speed for which the mean position error is less than one mean aerodynamic chord length, from 2.3 m/s to 4.1 m/s.

One of the reasons that the aligned tail-sitter may be able to withstand higher wind speeds than the normal tail-sitter is because of the stability of the equilibrium points. With higher wind speeds, the Dryden Turbulence Model produces larger fluctuations in wind speed and direction. When the aircraft is normal to the flow, it is hovering about an unsteady equilibrium point. The aircraft deviates significantly from its desired position as soon as there is a sudden change in wind direction, in general when there is a change of 10° over 2 s.

It follows that it is ideal for an aircraft to attempt to fly approximately aligned with the oncoming wind direction. Therefore, in the next section, we will further investigate flights in which the aircraft is controlled to try to maintain alignment with the wind.

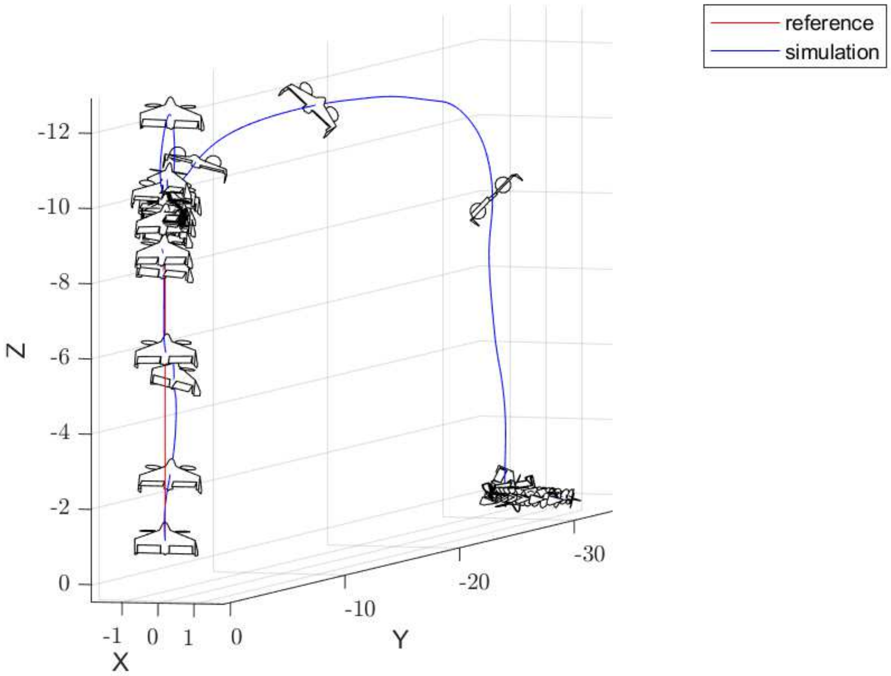

**Fig. 4.16**: Flight profile of aircraft flying with 2.5 m/s winds. Snapshots of position and attitude are taken every 1 s.

## 4.4 Wind Alignment Strategy

As shown in Section 4.3, taking off and hovering while aligned with the initial wind direction reduced the position RMSE from 4.1 m/s to 2.3 m/s. However, in real-world situations, it may not always be possible to take off aligned with the wind. Therefore, in this section, we evaluate the performance for different take-off orientations relative to the wind direction.

### 4.4.1 Implementation of Alignment Strategy

The same simulation framework is used as in previous sections, with the tail-sitter taking off and hovering at different wind speeds. In this section, we reconsider the original controller, shown in Figure 4.4, and modify the maneuver generator. In previous sections, the maneuver generator set the reference attitude $\mathbf{q}_{\mathrm{ref}}$ to be constant, at the initial attitude of the aircraft. Therefore, throughout the simulation, the tail-sitter attempted to maintain its initial orientation regardless of oncoming wind speed and direction.

Consider the diagram of the tail-sitter in Figure 4.18. The wind vector is denoted as $v_{wind}$, and its direction is denoted by $\theta_{\mathrm{w}}$. Angle $\beta$ denotes the misalignment angle between the aircraft and the wind direction. In this section, we modify $\mathbf{q}_{\mathrm{ref}}$, so that the desired at-

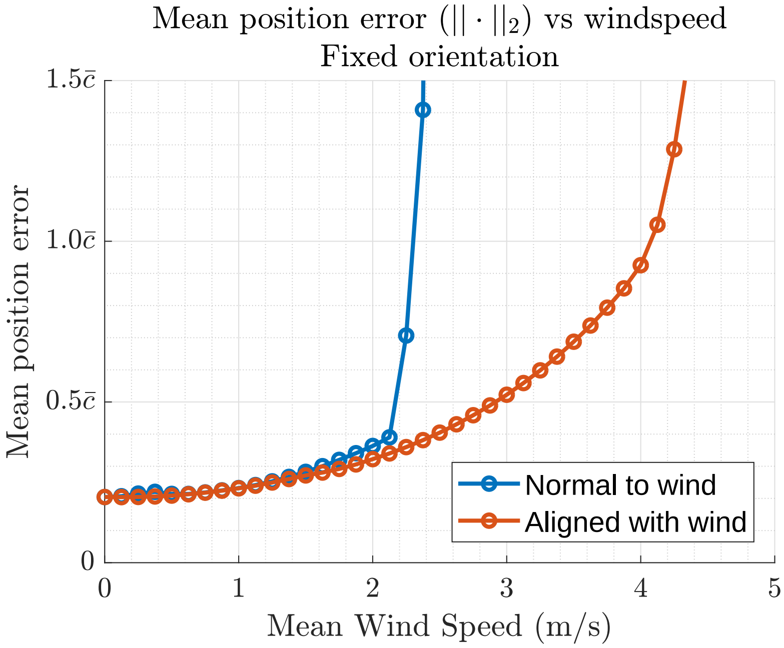

**Fig. 4.17**: RMSE of tail-sitter position error through take-off and hover vs wind speed.

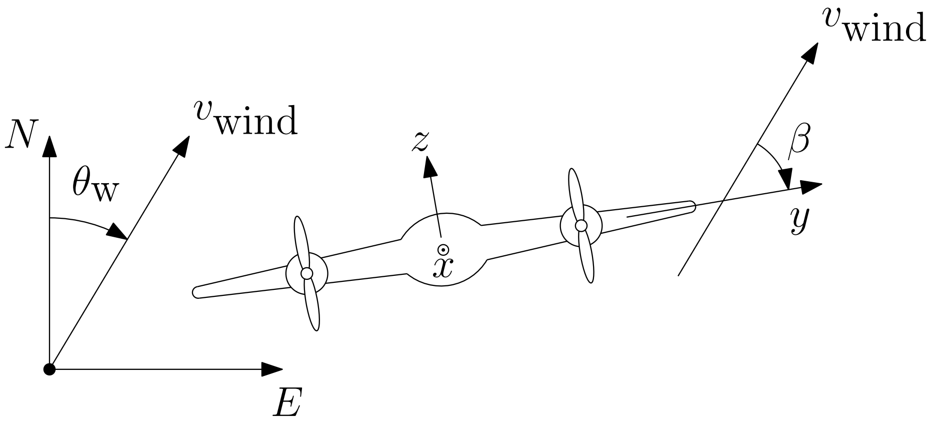

**Fig. 4.18**: Diagram of tail-sitter hovering in windy conditions.

titude of the aircraft is set with its nose up, and its body $y$-axis is aligned with the wind direction $\theta_\text{w}$. As such, throughout the simulation, the aircraft continuously attempts to align itself with the oncoming wind direction such that $\beta = 0°$, and we assume that the aircraft has knowledge of the wind direction, perhaps using a sensor such as the one discussed in Chapter 3. Whereas the feedforward compensator required both knowledge of wind speed and direction, this wind alignment strategy only requires knowledge of the wind direction, perhaps using a sensor such as the one presented in Chapter 3. Requiring only the wind direction reduces the uncertainty in the wind measurement, which should be beneficial.

The simulation was repeated under various conditions. The tail-sitter flew with five different initial alignments, ranging from the body aligned with the wind position $(\beta = 0°)$ to misaligned with the flow $(\beta = 90°)$, in $22.5°$ increments. Each simulation had wind speeds ranging from $0$–$6.5$ m/s, in $0.125$ m/s increments. These simulations were repeated with three levels of information provided to the aircraft controllers. First, exact instantaneous wind information was provided to the aircraft. Then, a moving average of the past $5$ s of wind information of wind data was provided to the controllers, and finally, the aircraft was only provided with the wind information at take-off.

### 4.4.2 Tracking with Exact Wind Knowledge

In the first instance, the controller was provided with exact instantaneous wind properties. This represents an ideal case, in which wind speed and direction can be measured on-board a UAV in real-time, with no error or delay. As seen in Figure 4.19, the maximum allowable wind speed for a successful run depends on the initial aircraft orientation on take-off. At wind speeds below $2$ m/s, there is a relatively small difference in position RMSE for all initial alignments.

Figure 4.20 provides two time histories of the aircraft, beginning misaligned by $90°$, attempting to align itself with the wind. In Figure 4.20(a), with a wind speed of $2.6$ m/s, the aircraft deviates horizontally from its desired path, but quickly recovers to its desired pose. In Figure 4.20(b), the wind speed is $4.0$ m/s, and the aircraft, attempting to align itself with the wind, deviates significantly from its desired position, and cannot correct its pose, causing it to crash into the ground.

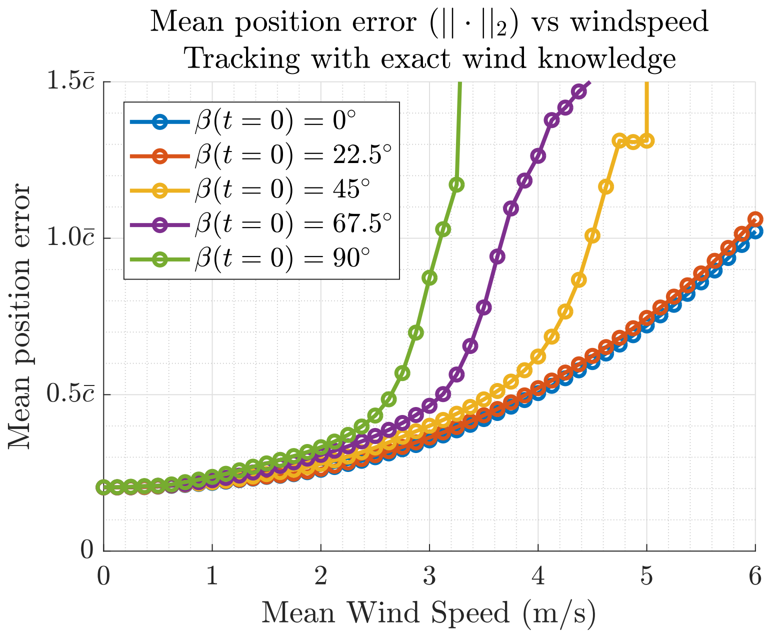

**Fig. 4.19**: RMSE of tail-sitter position error through take-off and hover vs initial wind speed at different initial alignments. Sensors are assumed to have exact knowledge of wind speed and direction.

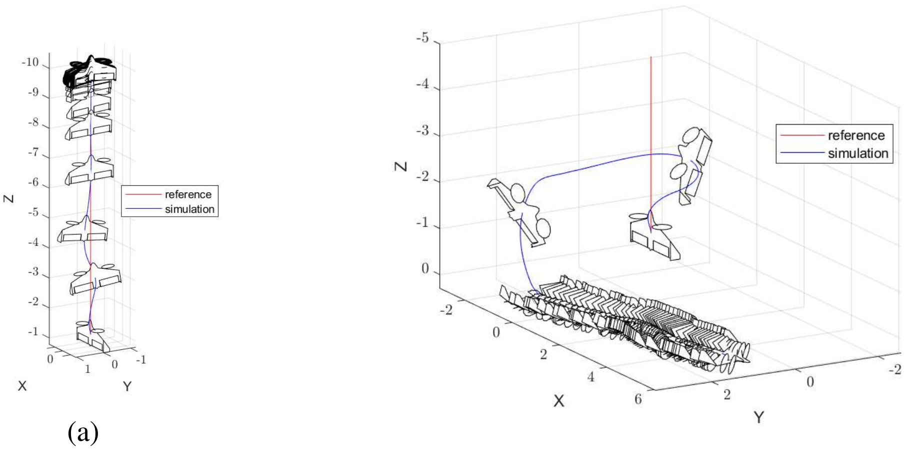

(a)

(b)

**Fig. 4.20**: Time profiles of aircraft, initially misaligned $90°$ with wind speeds of a) $2.6$ m/s, b) $4.0$ m/s. In both instances, snapshots of aircraft pose are taken every $1$ s.

At higher wind speeds, the RMSE was significantly impacted by the initial aircraft alignment. For an aircraft taking off initially normal to the oncoming flow direction, the RMSE exceeded one chord length at a wind speed of $3.1$ m/s, whereas an aircraft initially aligned with the oncoming flow was able to take off and hover in wind speeds of $6.0$ m/s before its RMSE exceeded one mean chord length. The small difference between $0°$ and $22.5°$ should be noted; if the aircraft is even approximately aligned with the wind direction, within $22.5°$, the difference in RMSE up to $6.0$ m/s is negligible. In the case where the aircraft took off $22.5°$ off of the wind direction, the aircraft was able to quickly align itself with the oncoming flow direction. However, at higher angles, as the aircraft attempted to align itself with the wind direction, the wind forces and moments caused the aircraft to deviate too far from its initial position for the tail-sitter to recover to its desired position.

It is also worth comparing the case for an initial misalignment of $90°$ in Figure 4.19, to the case in Figure 4.17 where the aircraft tries to maintain a misalignment of $90°$. In the former case, the aircraft performs successfully up to $3.1$ m/s and in the latter case, it only does so up until $2.2$ m/s. This indicates that the alignment maneuver is successful at increasing the operating range of the aircraft.

### 4.4.3 Tracking with Approximate Wind Knowledge

In Section 4.4.2, the tail-sitter's controller was provided with exact information of the oncoming wind speed and direction in order to reject wind disturbances and better align with the flow direction in real time. However, the discussion of sensor performance in Section 1.3.1 makes clear that exact knowledge of wind speed and direction unlikely in a real-world application. In this subsection, we examine the aircraft's performance under two hypothetical scenarios; one in which we provide a $5$ s moving average of the wind direction and another where we only provide known wind direction at take-off.

#### Tracking with Time-Averaged Wind Knowledge

We first consider the case where $5$ s averaged wind direction is provided. A sample of true wind direction and the time-averaged information is provided in Figure 4.21. This approximates the case where the sensor may have limited bandwidth and/or measurement delay.

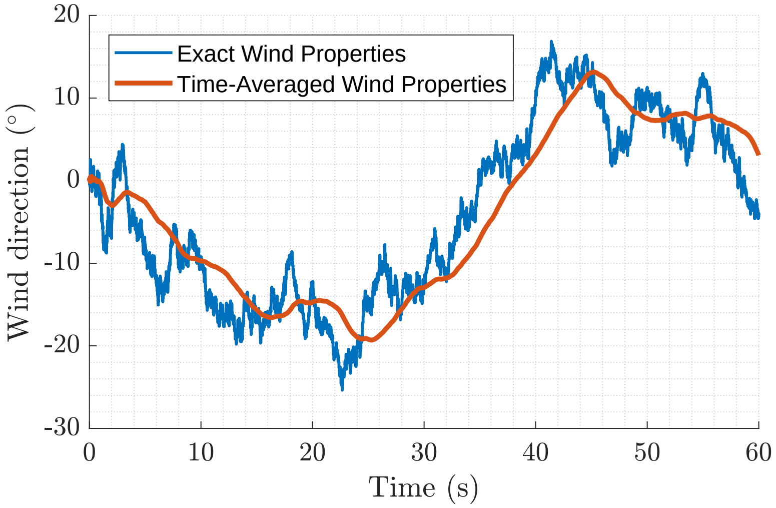

**Fig. 4.21**: Sample wind profile aimed North $(0^\circ)$ with $2.5$ m/s mean velocity. Exact direction, and an average of the previous $5$ s are shown.

These results, shown in Figure 4.22, are similar in trend to those of Figure 4.19. In fact, for an initial misalignment of $45^\circ$ or more, the results are nearly unchanged. Only for smaller misalignments are the results somewhat worsened with less precise knowledge of wind direction.

### Tracking with Take-Off Wind Knowledge

The same simulation was repeated while only providing the aircraft controllers with information about the wind direction at the moment of take off. Although on-board wind sensors cannot currently provide precise estimates of wind speed and direction, ground sensors are capable of this. On take-off, a ground-based anemometer could possibly measure the wind direction, and provide this information to the aircraft controller. Therefore, with this limited information, in every simulation, the tail-sitter attempts to align its body $y$-axis to the North, since the wind is nominally in that direction. As shown in Figure 4.21, this implies that the reference direction of the aircraft may be up to $22.5^\circ$ misaligned with the wind.

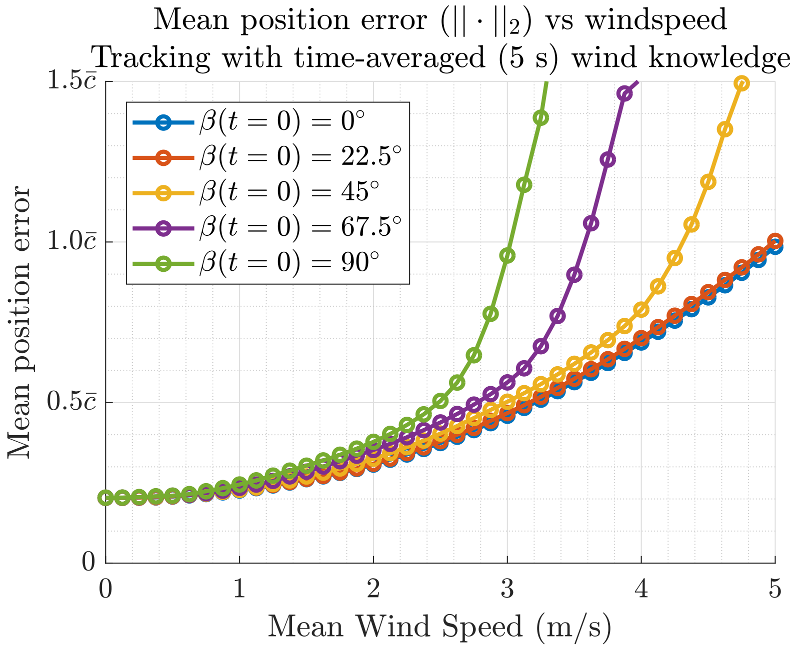

**Fig. 4.22**: RMSE of tail-sitter position error through take-off and hover vs initial wind speed at different initial alignments. Sensors are assumed to have knowledge of the average of the past 5 s of wind direction.

Once again, the results, shown in Figure 4.23, are similar in trend to those of Figure 4.19. For large initial misalignments of $\beta \geq 45°$, results are similar, while for small misalignments, the limited knowledge provides worse results.

### 4.4.4 Additional Results and Analysis

The results from Section 4.4.2 and Section 4.4.3 are further summarized in this section, by isolating the initial alignments and varying the amount of information provided to the tail-sitter controllers.

#### Take-off normal to wind direction

First, we consider the aircraft taking off normal to the wind direction, and rolling towards the wind direction, with each level of information provided to the controllers. Results are shown in Figure 4.24. Despite varying the quality of information provided to controllers, there was only a small change in the resulting performance. Since the limiting factor is the aircraft geometry and control authority, and sensor quality cannot affect these factors, the quality of wind sensors will have little impact on aircraft performance for a tail-sitter taking off approximately normal to oncoming wind.

### Take-off aligned with wind direction

Next, we consider the aircraft taking off aligned with the wind direction, and rolling towards the wind direction, with different levels of wind information provided to the controller. Results are shown in Figure 4.25. When the aircraft is aligned with the oncoming wind direction, the quality of information provided to the controllers has a significant impact on the position RMSE. With more precise data, the wind speed at which the RMSE exceeds one mean aerodynamic chord is increased by approximately $40\%$, from approximately $4.3$ m/s to $6.0$ m/s.

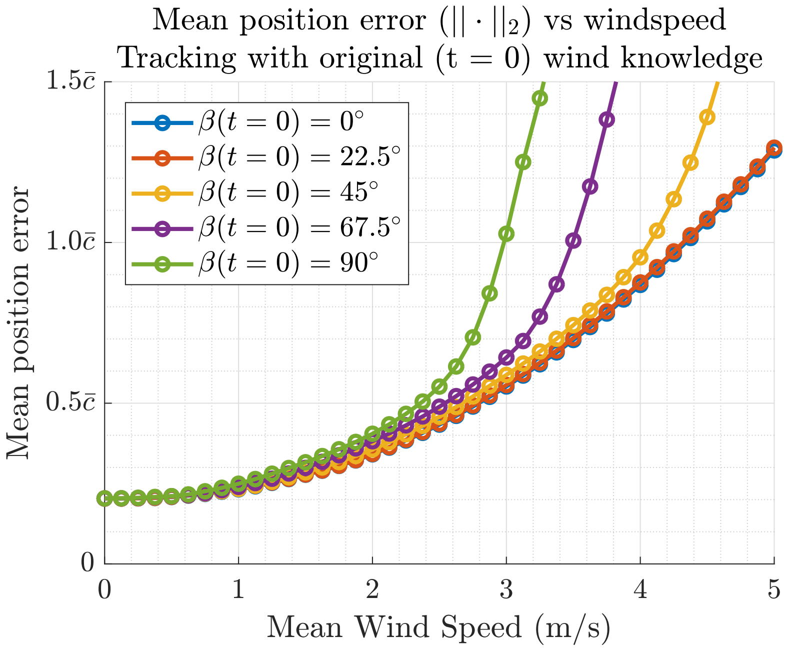

**Fig. 4.23**: RMSE of tail-sitter position error through take-off and hover vs initial wind speed at different initial alignments. Sensors are assumed to have knowledge of take off wind direction.

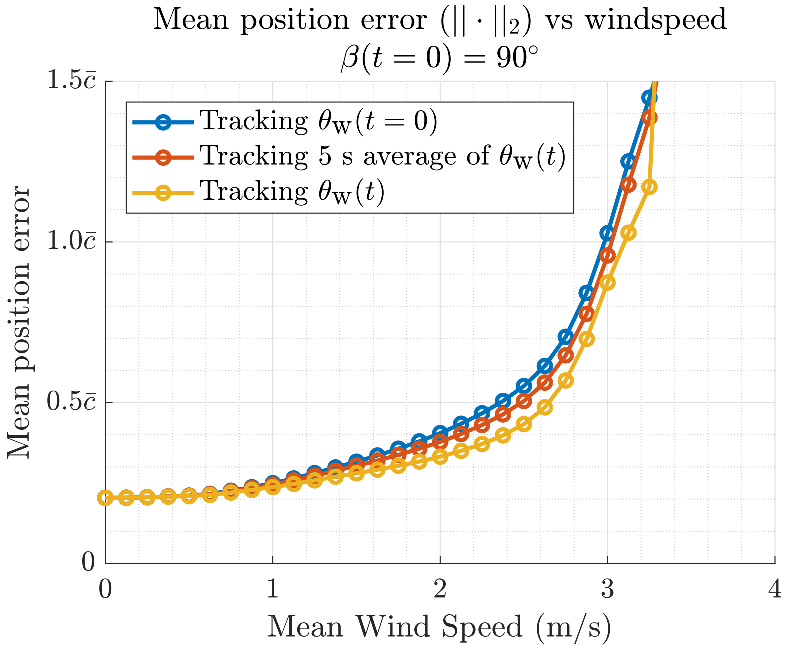

**Fig. 4.24**: RMSE of tail-sitter position error through take-off and hover vs initial wind speed, taking off normal to wind direction.

Beginning normal to the wind direction, with any quality of information, it is beneficial for the tail-sitter to attempt to align itself with the wind direction, in order to sustain higher wind speeds. However, as shown in Figure 4.25, improving the quality of wind sensors will drastically increase the aircraft's ability to handle strong winds.

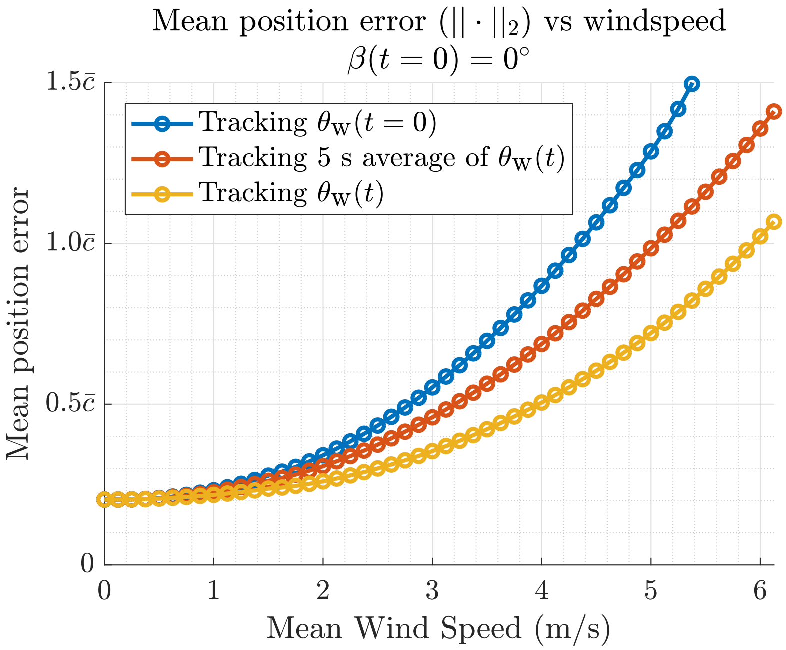

**Fig. 4.25**: RMSE of tail-sitter position error through take-off and hover vs initial wind speed, taking off aligned with wind direction.

# Chapter 5

# Conclusion

## 5.1 Main Conclusions

The focus of this thesis was to diminish the effects of wind disturbances on a hovering tail-sitter. This was separated into several tasks. First, wind tunnel measurements were performed to validate the work of [35]. At pitch angles, the model of [35] acts as an acceptable approximation to model th aircraft aerodynamics, as it predicted aerodynamic coefficients within 21% of measured values. However, at roll angles, the model of [35] was unable to accurately predict aerodynamic forces or moments. A new model building upon the work of [36] was proposed, which predicted forces within 30% and moments within 39% of measured data. Another conclusion of the rolling moment measurements was that there are two equilibrium points for the flat plate acrylic model; one stable equilibrium when the aircraft is aligned with the flow, and one unstable equilibrium point when the aircraft is normal to the flow.

One main issue raised in the introduction was the lack of available sensors to properly estimate oncoming wind speed and direction. In this thesis, we proposed a novel method to estimate oncoming wind speed and direction. By embedding one pair of pressure taps near the nose of a flat plate acrylic model, and another pair of pressure taps near the geometric centre of the plate, to measure the pressure difference across the surface, we were able to estimate wind speed within $10\%$, and wind direction within $10^\circ$ of real values, when considering winds between $40 - 90^\circ$ roll angles relative to the aircraft.

In Chapter 4, two methods were considered to reduce the position error for a climb and hover maneuver in the MATLAB Simulink framework. First, with the addition of feedforward control, we learned that the use of feedforward control could be used to slightly reduce position error through a given flight. However, in simulations, feedforward control was not able to significantly increase the maximum wind speed at which the aircraft could successfullly perform the maneuver. Once the tail-sitter was subjected to strong enough wind speeds, the elevons were at their maximum deflections, and did not have enough control authority to provide moments strong enough to maintain the aircraft's position.

A controller to align the aircraft with the wind direction was examined next. As suggested in the user's manual for the X-Vert tail-sitter, it was found here that taking off and hovering while aligned with the wind direction both reduced position error and increased the range of wind speeds under which the aircraft could fly successfully. This is likely a result of both the aircraft experiencing lower forces when aligned with the wind, and hovering about a stable equilibrium point rather than an unstable one.

Since the aircraft was more stable when aligned with the wind direction, we attempted to align the aircraft with the wind direction after starting from various initial alignments. Furthermore, we varied the quality of information provided to the aircraft controller. If taking off normal to the wind direction, it is beneficial for the aircraft to attempt to align itself with the the flow, rather than maintaining its initial attitude. When misaligned on take-off, the level of knowledge provided to the aircraft controllers has a negligible impact on performance. Taking off while approximately aligned with wind direction, within $22.5^\circ$, provided much better performance. When aligned on take-off, with better quality information provided to the controllers, the aircraft was able to perform well in stronger winds, as expected.

## 5.2 Recommendations Future Work

There exist a number of possible avenues for future work, both on the fluid dynamics and control systems aspects of the project.

We noted in Chapter 2 that little information currently exists for flat plates at oblique angles. Data exists for rectangular and delta-wing shapes for pitch angles, and occasionally roll angles, but not for combinations of pitch and roll angles. Especially for tail-sitter aircraft, which can take off vertically, then transition to horizontal cruising, the effective velocity of the aircraft will often have non-negligible components in the body $x$, $y$, and $z$ directions.

Furthermore, there is a growing need for aerodynamic coefficients for flat plates with ultra-low aspect ratios. Currently, there is very limited data available in literature for flat plates with aspect ratios below $0.4$–$0.5$. As shown in Section 2.5, when an aircraft with aspect ratio $\mathit{AR} = 3.2$ is hovering, its rolling moment will be similar to the pitching moment for a flat plate with aspect ratio $\mathit{AR} = \frac{1}{3.2}$. With the emergence of drones and agile UAVs, modelling aerodynamics of flat plates with an aspect ratio well below $0.5$ should be a priority, where leading edge vortices have a more significant impact on the aerodynamics.

The measured aerodynamic coefficients, as well as those found in literature, tend to focus on steady-state results. However, agile aircraft, and transitioning tail-sitters, are not in steady configurations. There will be a non-negligible transient force and moment for these aircraft. In order to better model the aerodynamic forces and moments on aircraft, or even flat plates, further research must be done to determine these values.

Although the novel method to determine wind direction with two pairs of pressure taps provided promising results, it had several drawbacks. The sensing method proposed only worked for wind directions between $40 - 90°$ and wind speeds above $7.5$ m/s. As the aircraft became more aligned with the wind direction at angles between $0 - 40°$, the surface polynomial could not adequately estimate wind direction. Furthermore, this method was only able to estimate wind direction if it lies exactly in the body $y$-$z$ plane. In real applications, the tail-sitter will be subjected to more complex flows. Therefore, if this method were to be further pursued, it would have to be evaluated at combinations of roll and pitch angles. It is likely that additional pairs of pressure taps would be required to determine combinations of angles.

The results obtained in Chapter 4 were produced using MATLAB Simulink. Although these results can provide promising steps forward for controlling a tail-sitter in strong winds, these results may not translate directly to real-world applications. While wind sensor noise was modelled somewhat in Section 4.4.3, the proposed controller should be implemented onto the X-Vert's autopilot hardware and tested in an outdoor environment to validate the simulation results.

# References

[1] D. W. Murphy and J. Cycon, “Applications for mini VTOL UAV for law enforcement,” in *Sensors, C3I, Information, and Training Technologies for Law Enforcement*, vol. 3577. International Society for Optics and Photonics, 1999, pp. 35–44.

[2] S. S. Dhaliwal and A. Ramirez-Serrano, “Control of an unconventional VTOL UAV for search and rescue operations within confined spaces based on the MARC control architecture,” in *2009 IEEE International Workshop on Safety, Security Rescue Robotics (SSRR 2009)*. IEEE, 2009, pp. 1–6.

[3] L. Merino and A. Ollero, “Forest fire perception using aerial images in the COMETS Project,” in *2002 IEEE/RSJ Int. Conf. on Intelligent Robots and Systems-IROS 2002. Proc. Workshop WS6 Aerial Robotics*, 2002, pp. 11–22.

[4] “Drones: Reporting for work.” [Online]. Available: https://www.goldmansachs.com/insights/technology-driving-innovation/drones/

[5] E. Bulka and M. Nahon, “Automatic control for aerobatic maneuvering of agile fixed-wing UAVs,” *Journal of Intelligent & Robotic Systems*, vol. 93, no. 1, pp. 85–100, Feb 2019. [Online]. Available: https://doi.org/10.1007/s10846-018-0790-z

[6] 2019. [Online]. Available: https://wingtra.com/mapping-drone-wingtraone/

[7] RC-Helicopter.co.uk, “Getting started in RC helicopters,” 2019. [Online]. Available: http://www.rc-helicopter.co.uk/

[8] N. K. Tran, E. Bulka, and M. Nahon, “Quadrotor control in a wind field,” in *2015 International Conference on Unmanned Aircraft Systems (ICUAS)*. IEEE, 2015, pp. 320–328.

[9] U. Ozdemir, Y. O. Aktas, A. Vuruskan, Y. Dereli, A. F. Tarhan, K. Demirbag, A. Erdem, G. D. Kalaycioglu, I. Ozkol, and G. Inalhan, “Design of a commercial hybrid VTOL UAV system,” *Journal of Intelligent & Robotic Systems*, vol. 74, no. 1, pp. 371–393, 2014. [Online]. Available: https://doi.org/10.1007/s10846-013-9900-0

[10] Flickr, “Spanish EAV-8B Harrier II+ “Cobra”,” 2015. [Online]. Available: https://www.flickr.com/photos/galeriadechato/27448607244/in/photostream/

[11] K. Muraoka, N. Okada, D. Kubo, and M. Sato, “Transition flight of quad tilt wing VTOL UAV,” in *28th Congress of the International Council of the Aeronautical Sciences*, 2012.

[12] C. A. Mitchell and B. J. Vogel, “The canard rotor wing (CRW) aircraft–a new way to fly,” in *AIAA International Air and Space Symposium and Exposition: The Next 100 Years*, 2003, p. 2517.

[13] W. F. Chana and J. F. S. Coleman, “World’s first VTOL airplane Convair/Navy XFY-1 Pogo,” *SAE Transactions*, vol. 105, pp. 1261–1266, 1996. [Online]. Available: http://www.jstor.org/stable/44725614

[14] N. Knoebel, S. Osborne, D. Snyder, T. Mclain, R. Beard, and A. Eldredge, “Preliminary modeling, control, and trajectory design for miniature autonomous tailsitters,” in *AIAA Guidance, Navigation, and Control Conference and Exhibit*. Reston, Virigina: American Institute of Aeronautics and Astronautics, Aug 2006. [Online]. Available: http://arc.aiaa.org/doi/10.2514/6.2006-6713

[15] K. Atherton, “Bell takes tailsitter route to VTOL cargo drones,” *Aviation Week*, 2019. [Online]. Available: https://aviationweek.com/future-aerospace/bell-takes-tailsitter-route-vtol-cargo-drones

[16] W. M. O. C. for Maritime Meteorology and W. M. Organization, “The Beaufort scale of wind force (technical and operational aspects),” pp. 21–22, 1970.

[17] G. V. Raffo, M. G. Ortega, and F. R. Rubio, "An integral predictive/nonlinear $\mathcal{H}_\infty$ control structure for a quadrotor helicopter," *Automatica*, vol. 46, no. 1, pp. 29–39, 2010.

[18] D. Cabecinhas, R. Cunha, and C. Silvestre, "Experimental validation of a globally stabilizing feedback controller for a quadrotor aircraft with wind disturbance rejection," in *2013 American Control Conference*. IEEE, 2013, pp. 1024–1029.

[19] H. L. Dryden, "A review of the statistical theory of turbulence," *Quarterly of Applied Mathematics*, vol. 1, no. 1, pp. 7–42, 1943.

[20] J. Steck, K. Rokhsaz, U. Pesonen, B. Singh, and R. Chandramohan, "Effect of turbulence on an adaptive dynamic inverse flight controller," in *AIAA Infotech@Aerospace*. AIAA, 2005. [Online]. Available: https://arc.aiaa.org/doi/abs/10.2514/6.2005-7038

[21] C. Hancer, K. T. Oner, E. Sirimoglu, E. Cetinsoy, and M. Unel, "Robust hovering control of a quad tilt-wing UAV," in *IECON 2010 - 36th Annual Conference on IEEE Industrial Electronics Society*. IEEE, Nov 2010, pp. 1615–1620.

[22] C. Zhang, X. Zhou, H. Zhao, A. Dai, and H. Zhou, "Three-dimensional fuzzy control of mini quadrotor UAV trajectory tracking under impact of wind disturbance," in *2016 International Conference on Advanced Mechatronic Systems (ICAMechS)*, 2016, pp. 372–377.

[23] S. Waslander and C. Wang, "Wind disturbance estimation and rejection for quadrotor position control," in *AIAA Infotech @ Aerospace*. IEEE, 2009, p. 1983.

[24] D. Yeo, N. Sydney, D. A. Paley, and D. Sofge, "Onboard flow sensing for downwash detection and avoidance with a small quadrotor helicopter," in *AIAA Guidance, Navigation, and Control Conference*, 2015, p. 1769.

[25] K. Oosting and S. L. Dickerson, "Simulation of a high-speed lightweight arm," in *Proceedings. 1988 IEEE International Conference on Robotics and Automation*. IEEE, 1988, pp. 494–496.

[26] N. K. Tran, "Modeling and control of a quadrotor in a wind field," Master's thesis, McGill University, Montreal, Quebec, 2015.

[27] R. H. Stone, P. Anderson, C. Hutchison, A. Tsai, P. Gibbens, and K. C. Wong, "Flight testing of the T-Wing tail-sitter unmanned air vehicle," *Journal of Aircraft*, vol. 45, no. 2, pp. 673–685, 2008. [Online]. Available: https://doi.org/10.2514/1.32750

[28] R. H. Stone, "Control architecture for a tail-sitter unmanned air vehicle," in *2004 5th Asian Control Conference*, IEEE. IEEE, 2004, pp. 736–744. [Online]. Available: http://ieeexplore.ieee.org/document/1426743/

[29] R. H. Stone and G. Clarke, "Optimization of transition maneuvers for a tail-sitter unmanned air vehicle (UAV)," in *Australian International Aerospace Congress*, vol. 4. Citeseer, 2001.

[30] R. H. Stone, "The T-wing tail-sitter research UAV," in *2002 Biennial International Powered Lift Conference and Exhibit*, 2002, p. 5970.

[31] D. Kubo and S. Suzuki, "Tail-sitter vertical takeoff and landing unmanned aerial vehicle: transitional flight analysis," *Journal of Aircraft*, vol. 45, no. 1, pp. 292–297, 2008.

[32] Y. Jung and D. H. Shim, "Development and application of controller for transition flight of tail-sitter UAV," *Journal of Intelligent & Robotic Systems*, vol. 65, no. 1, pp. 137–152, 2012. [Online]. Available: https://doi.org/10.1007/s10846-011-9585-1

[33] K. Kita, A. Konno, and M. Uchiyama, "Transition between level flight and hovering of a tail-sitter vertical takeoff and landing aerial robot," *Advanced Robotics*, vol. 24, no. 5-6, pp. 763–781, 2010.

[34] T. Matsumoto, K. Kita, R. Suzuki, A. Oosedo, K. Go, Y. Hoshino, A. Konno, and M. Uchiyama, "A hovering control strategy for a tail-sitter VTOL UAV that increases stability against large disturbance," in *2010 IEEE International Conference on Robotics and Automation*. IEEE, 2010, pp. 54–59. [Online]. Available: http://ieeexplore.ieee.org/document/5509183/

[35] R. Chiappinelli and M. Nahon, "Modeling and control of a tailsitter UAV," in *2018 International Conference on Unmanned Aircraft Systems (ICUAS)*. IEEE, 2018, pp. 400–409.

[36] W. Khan and M. Nahon, "Modeling dynamics of agile fixed-wing UAVs for real-time applications," in *2016 International Conference on Unmanned Aircraft Systems (ICUAS)*. IEEE, 2016, pp. 1303–1312.

[37] I. Wygnanski and B. G. Newman, "General description and calibration of the McGill 3ft x 2ft low speed wind tunnel," 1961.

[38] J. Anderson, *Fundamentals of Aerodynamics*. McGraw-Hill, 2001.

[39] J. Barlow, W. Rae, and A. Pope, *Low-Speed Wind Tunnel Testing*. Wiley, 1999.

[40] J. A. Hoffmann, "Effects of freestream turbulence on the performance characteristics of an airfoil," *AIAA Journal*, vol. 29, no. 9, pp. 1353–1354, 1991.

[41] G. E. Torres and T. J. Mueller, "Low aspect ratio aerodynamics at low Reynolds numbers," *AIAA Journal*, vol. 42, no. 5, pp. 865–873, 2004.

[42] R. Fail, R. C. W. Eyre, and J. A. Lawford, *Low-speed experiments on the wake characteristics of flat plates normal to an air stream*. HM Stationery Office, 1959.

[43] W. Humphries and J. H. Vincent, "Near wake properties of axisymmetric bluff body flows," *Applied Scientific Research*, vol. 32, no. 6, pp. 649–669, 1976. [Online]. Available: https://doi.org/10.1007/BF00384126

[44] P. W. Bearman, "An investigation of the forces on flat plates normal to a turbulent flow," *Journal of Fluid Mechanics*, vol. 46, no. 1, p. 177–198, 1971.

[45] J. Nedić, B. Ganapathisubramani, and J. C. Vassilicos, "Drag and near wake characteristics of flat plates normal to the flow with fractal edge geometries," *Fluid Dynamics Research*, vol. 45, no. 6, p. 061406, 2013.

[46] F. H. Abernathy, "Flow over an inclined plate," *Journal of Basic Engineering*, vol. 84, no. 3, pp. 380–388, 1962. [Online]. Available: https://doi.org/10.1115/1.3657331

[47] J. Hunt, E. Poulton, and J. Mumford, “The effects of wind on people; new criteria based on wind tunnel experiments,” *Building and Environment*, vol. 11, no. 1, pp. 15 – 28, 1976. [Online]. Available: http://www.sciencedirect.com/science/article/pii/0360132376900159

[48] W. Melbourne, “Criteria for environmental wind conditions,” *Journal of Wind Engineering and Industrial Aerodynamics*, vol. 3, no. 2, pp. 241 – 249, 1978. [Online]. Available: http://www.sciencedirect.com/science/article/pii/0167610578900132

[49] W. D. Lubitz, “Impact of ambient turbulence on performance of a small wind turbine,” *Renewable Energy*, vol. 61, pp. 69 – 73, 2014. [Online]. Available: http://www.sciencedirect.com/science/article/pii/S0960148112004855